ADVANCED FUNCTIONAL MATERIALS
www.afm-journal.de

Fused Thiophene Semiconductors: Crystal Structure–Film Microstructure Transistor Performance Correlations

Jangdae Youn, Sumit Kewalramani, Jonathan D. Emery, Yanrong Shi, Shiming Zhang, Hsiu-Chieh Chang, You-jhih Liang, Chia-Ming Yeh, Chieh-Yuan Feng, Hui Huang, Charlotte Stern, Liang-Hsiang Chen, Jia-Chong Ho, Ming-Chou Chen, Michael J. Bedzyk,* Antonio Facchetti,* and Tobin J. Marks**

The molecular packing motifs within crystalline domains should be a key determinant of charge transport in thin-film transistors (TFTs) based on small organic molecules. Despite this implied importance, detailed information about molecular organization in polycrystalline thin films is not available for the vast majority of molecular organic semiconductors. Considering the potential of fused thiophenes as environmentally stable, high-performance semiconductors, it is therefore of interest to investigate their thin film microstructures in relation to the single crystal molecular packing and OTFT performance. Here, the molecular packing motifs of several new benzo[*d*,*d*′]thieno[3,2-*b*;4,5-*b*′]dithiophene (BTDT) derivatives are studied both in bulk 3D crystals and as thin films by single crystal diffraction and grazing incidence wide angle X-ray scattering (GIWAXS), respectively. The results show that the BTDT derivative thin films can have significantly different molecular packing from their bulk crystals. For phenylbenzo[*d*,*d*′]thieno[3,2-*b*;4,5-*b*′]dithiophene (P-BTDT), 2-biphenylbenzo[*d*,*d*′]thieno-[3,2-*b*;4,5-*b*′]dithiophene (Bp-BTDT), 2-naphthalenylbenzo[*d*,*d*′]thieno[3,2-*b*;4,5-*b*′]dithiophene (Np-BTDT), and bisbenzo[*d*,*d*′]thieno[3,2-*b*;4,5-*b*′]dithiophene (BBTDT), two lattices co-exist, and are significantly strained versus their single crystal forms. For P-BTDT, the dominance of the more strained lattice relative to the bulk-like lattice likely explains the high carrier mobility. In contrast, poor crystallinity and surface coverage at the dielectric/substrate interface explains the marginal OTFT performance of seemingly similar PF-BTDT films.

1. Introduction

Over the past decade, the field of organic thin-film transistors (OTFTs) has seen remarkable progress,[1–3] and a number of products based on organic electronic circuitry are already on the verge of commercialization.[4] However, at this exciting moment, there remain critical challenges in finding organic semiconductors with electrical performance, reliability, and processing windows surpassing amorphous silicon. These challenges must be addressed to propel the widespread adoption of organic electronics into mass production. Among several classes of organic semiconductor materials, acene-based small molecules,[5] most notably pentacene,[6,7] have long been of prime interest due to their excellent charge transport properties. However, the environmental instability of acene-based organic semiconductors critically limits their applicability in electronic circuitry.[8] For this reason, many research groups have sought to realize new molecular building blocks that are environmentally stable, and, at the same time, exhibit efficient charge transport. Fused thiophene

Dr. J. Youn, Dr. Y. Shi, Dr. S. M. Zhang, Dr. H. Huang, C. Stern, Prof. A. Facchetti, Prof. T. J. Marks
Department of Chemistry and the Materials Research Center
Northwestern University
2145 Sheridan Rd., Evanston, IL 60208-3113, USA
E-mail: a-facchetti@northwestern.edu; t-marks@northwestern.edu
Dr. S. Kewalramani, J. D. Emery, Prof. M. J. Bedzyk
Department of Materials Science and Engineering
Department of Physics and Astronomy
Northwestern University
2220 Campus Dr., Evanston, IL 60208-3113, USA
E-mail: bedzyk@northwestern.edu
H.-C. Chang, Y.-J. Liang, C.-M. Yeh, C.-Y. Feng, Prof. M.-C. Chen
Department of Chemistry
National Central University
Jhong-Li, Taiwan, 32054, R.O.C.
E-mail: mcchen@ncu.edu.tw
Dr. L.-H. Chen, Dr. J.-C. Ho
Process Technology Division
Display Technology Center
Industrial Technology Research Institute
Chung Hsing Rd., Chutung, Hsinchu, Taiwan, 31040, R.O.C.

DOI: 10.1002/adfm.201203439

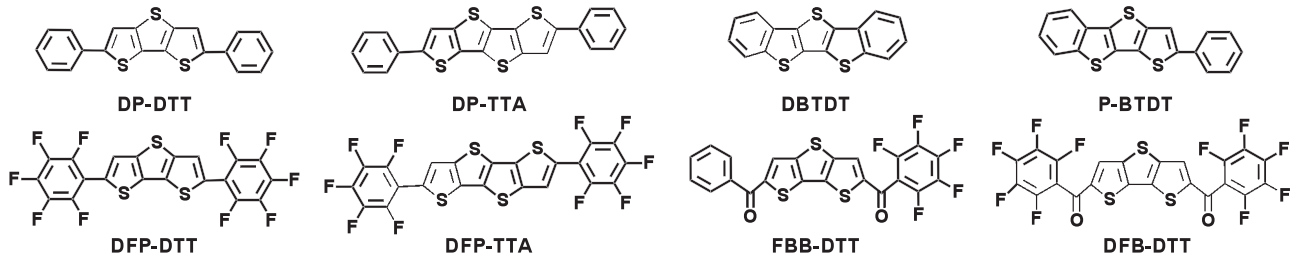

Scheme 1. Examples of fused oligothiophene semiconductors used in TFTs.

derivatives[2,9–14] offer a potential solution to this challenge, owing to their combination of sufficiently high-lying excited states and high ionization potentials to suppress photo-oxidation,[11] and bulk single crystal packing motifs which are very similar to that of pentacene. Among organic semiconductor materials for p-channel devices, several fused thiophene derivatives with increased numbers of thiophene rings exhibit excellent charge transport performance. For example, **DP-DTT**,[14] **DP-TTA**,[12] and **DBTDT**[13] exhibit hole mobilities as high as 0.42, 0.14, and 0.51 $cm^2 V^{-1} s^{-1}$, respectively (**Scheme 1**). To date our laboratory has developed a number of distinctive fused thiophene molecules for TFT applications. Among them, a series of fused thiophenes based on benzo[*d,d'*]thieno[3,2-*b*;4,5-*b'*]dithiophene (**BTDT**) exhibit good environmental stability as well as high mobilities. Specifically, the phenyl end-capped derivative **P-BTDT** exhibits a carrier mobility as high as 0.70 $cm^2 V^{-1} s^{-1}$.[9]

While specific optoelectronic properties of organic semiconductors at the parent molecule level are a necessary factor in achieving high TFT performance, actual device operation is affected by many parameters related to film microstructure. For example, the intrinsic packing of the molecules within the unit cell,[3,15–17] as well as the size, density, and orientation of crystalline domains,[18] the type of domain boundaries,[19] and the nature of the semiconductor-gate dielectric interface.[20] Specifically, the local packing of molecules determines intermolecular orbital overlap and may also influence the crystalline domain size. Similarly, the connectivity between adjacent domains influences the paths taken by charge carriers through films.[21] In particular, the microstructure of the first monolayers above the dielectric plays a critical role in determining OTFT performance because the charge transport is highly localized in the channel within 3–5 nm of this interface.[21]

Unfortunately, with few exceptions,[3,15–17] detailed information on the aforementioned issues is unavailable for most small molecule organic semiconductor films. As a result, discussions of TFT charge transport properties are often based on information extrapolated from the bulk single crystal structures. However, in the few cases where these structural factors have been scrutinized, such assumptions have been proven to sometimes be inaccurate, and it is now known that molecular packing in thin films may differ significantly from that in the bulk crystal structures, especially near the dielectric interface. For example, in thin film form, both tetraceno[2,3-b]thiophene[17] and pentacene[16] exhibit a local molecular packing distinctly different from that in the bulk crystal. These observations highlight the necessity of obtaining microstructural details for thin organic films.

In this contribution, the molecular packing motifs of five newly synthesized **BTDT**[9] derivatives (**Scheme 2**), are studied both in bulk single crystals and in thin films by single crystal diffraction and grazing incidence wide angle X-ray scattering (GIWAXS). We first introduce the new **BTDT** molecules and describe their thermal, optical, and electrochemical properties. We then compare the bulk and thin film structures by analyzing single-crystal X-ray diffraction and GIWAXS data. Lastly, the effect of thin film microstructure on TFT performance is discussed. The results indicate that these **BTDT** derivatives have different molecular packing in thin films versus the bulk crystals. In the case of **P-BTDT**, **Bp-BTDT**, **Np-BTDT**, and **BBTDT**, it will be seen that two types of lattices coexist, and that these are slightly strained compared to their bulk crystal forms. In contrast, for **PF-BTDT** films, a single lattice is observed, however, this lattice has no apparent correspondence to the bulk crystal form. For **P-BTDT**, which yields the best performing TFTs of the series, the dominance of the more strained lattice relative to the bulk-like lattice may explain the excellent charge transport properties. On the other hand, poor crystallinity and poor surface coverage at the substrate interface explains the poor device performance of **PF-BTDT** films.

2. Results

2.1. Synthesis

Details of the various **BTDT** syntheses can be found in the Supporting Information or previous literature.[9] Briefly, the

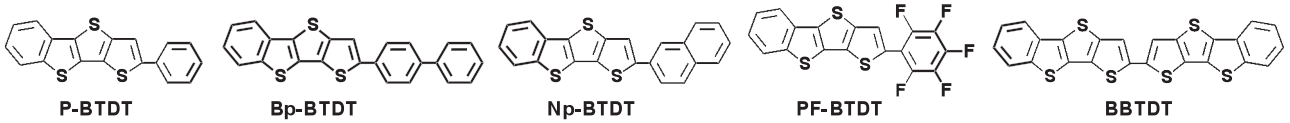

Scheme 2. Chemical structures of the benzo[*d,d'*]thieno[3,2-*b*;4,5-*b'*] dithiophene (**BTDT**) semiconductors examined in this study.

DOI: 10.1002/adfm.201203439

Table 1. Thermal, optical, and electrochemical properties of BTDT derivatives. All potentials reported are referenced to an Fc^+/Fc internal standard (at +0.6 V).

Compound	DSC Tm [°C]	TGA °C, [5%]	UV-Vis λ_{max} [a)] [nm]	Reduction Potential [b)] [V]	Oxidation Potential [b)] [V]	ΔE_{gap} [eV] (UV) [a)]	ΔE_{gap} [eV] (DPV) [b)]
P-BTDT	269	287	358	–1.98	1.39	3.21	3.37
PF-BTDT	316	247	351	–1.75	1.61	3.22	3.36
Bp-BTDT	392	402	369	–1.98	1.30	3.07	3.28
Np-BTDT	299	366	369	–1.96	1.31	3.08	3.27
BBTDT	461	471	411	–1.75	1.14	2.74	2.89

[a)] In *o*-$C_6H_4Cl_2$; [b)] In *o*-$C_6H_4Cl_2$ at 60 °C.

functionalizations of **BTDT** molecule were carried out according to the synthetic protocols shown in Scheme S1 (Supporting Information). **BTDT** is first deprotonated with *n*-BuLi, and then alkylstannylated to generate **BTDT-SnR$_3$**. Next, this compound was straightforwardly coupled with the corresponding aryl bromide to produce **P-BTDT, Bp-BTDT**, **Np-BTDT**, **PF-BTDT**, and **BBTDT** in 46%, 85%, 82.5%, 35%, and 45% yield, respectively, via a Stille coupling protocol. **PF-BTDT** can be also obtained by deprotonating **BTDT** in the presence of C_6F_6 in 28% yield. All compounds were characterized by conventional chemical and physical methodologies.

2.2. Thermal, Optical, and Electrochemical Properties of BTDT Derivatives

For the five **BTDT** derivatives, differential scanning calorimetry (DSC) scans reveal sharp endotherms above 269 °C, and thermogravimetric analysis (TGA) plots demonstrate weight loss (≈5%) only on heating above 287 °C, except for fluorinated **PF-BTDT**, as summarized in **Table 1**. Lower melting points and lower weight loss temperatures are observed for the **BTDT** derivatives having lower molecular weights. However, **PF-BTDT** exhibits a 5% weight loss temperature ≈247 °C, lower than that of **P-BTDT**, indicating higher volatility due to the fluorocarbon substitution.[22] The optical absorption spectra of **Bp-BTDT**, **Np-BTDT**, and **BBTDT** in *o*-$C_6H_4Cl_2$ solution (Supporting Information Figure S1) are slightly red-shifted (λ_{max} > 369 nm), relative to that of the **P-BTDT** (λ_{max} ≈ 358 nm). In contrast, the absorption spectrum of **PF-BTDT** is slightly blue-shifted relative to **P-BTDT**. This result is consistent with the observation that biphenyl, naphthalenyl, and benzo[*d*,*d*]thieno[3,2-*b*;4,5-*b*]dithiophenyl substituted **BTDTs** have greater electronic delocalization than does phenyl substituted **BTDT**. The stability of these compounds against photooxidation was also investigated by monitoring the decay of the optical absorption maxima in aerated *o*-$C_6H_4Cl_2$ solutions exposed to a white fluorescent lamp light at room temperature. No decomposition is observed after 4-5 days of continuous illumination.

Differential pulse voltammograms (DPVs; see Supporting Information for details) of the **BTDT** derivatives were recorded in dichlorobenzene at 60 °C and the results are summarized in Table 1. The DPVs of **Bp-BTDT** and **Np-BTDT** exhibit oxidation peaks close to +1.30 V and reduction peaks at –1.98 V. The oxidation potential is shifted to smaller values (easier oxidizing) than that of **P-BTDT** (E_{ox} = +1.39 V), which is attributable to aryl substituent conjugative effects. Similarly, the oxidation potential of more conjugated **BBTDT** (E_{ox} = +1.14 V) is shifted to less positive values, while the reduction potential is displaced to a less negative value (E_{red} = –1.75 V). In contrast, both E_{ox} = +1.61 V; and E_{red} = –1.75 V of **PF-BTDT** are shifted to more positive values (more difficult oxidizing) than those of **P-BTDT** (E_{ox} = +1.39 V; E_{red} = –1.98V) without a significant difference in oxidation and reduction potential, consistent with well-known electron-withdrawing group (EWG) effects. The difference in oxidation and reduction potential obtained from the DPV data (**Figure 1**) rise in the order: **BBTDT** (2.89 eV) < **Bp-BTDT** ≈ **Np-BTDT** (3.27 eV) < **P-BTDT** (3.37 eV) ≈ **PF- BTDT** (3.36 eV), in good agreement with the values obtained from optical spectroscopy (Table 1). HOMO energies (E_{HOMO}) were estimated using equation, $E_{HOMO} = -(4.20 + E_{ox})$; assuming ferrocene/ferrocenium oxidation at 4.8 eV.[23]

The low HOMO energies for the **BTDT** derivatives correlate their UV photooxidative stability. In addition, the fluoroaryl substitution in **PF-BTDT** substantially lowers both the HOMO and LUMO energies versus those of **P-BTDT**. Note that the HOMO energies of **BTDT** derivatives are close to the work function of a clean fresh gold surface (–5.1 eV), although the gold work function can be as high as –4.3 eV due to contaminants adsorbed under ambient conditions. Nevertheless, it can be concluded that the present **BTDT** compounds should have relatively small hole injection barriers from gold electrodes for p-type TFT operation.

2.3. Single Crystal Structural Analysis

Before examining the thin film structure of **BTDTs**, the bulk single crystal structures are analyzed in order to establish a referential basis for further discussion. The crystal structures and lattice parameters obtained from single crystal diffraction measurements followed by crystallographic refinement calculations for each of the **BTDTs** are summarized in **Table 2** below. Details of the single crystal diffraction measurements and crystallographic refinement are summarized in Tables S1-S5. The local packing parameters known to affect the

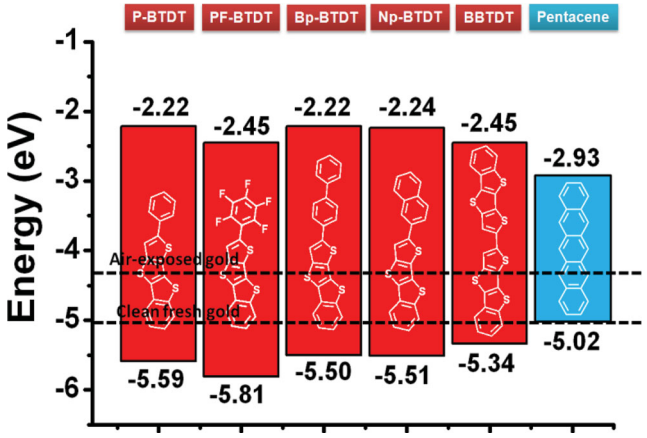

Figure 1. DPV-derived HOMO and LUMO energy levels of BTDT semiconductors compared to the work functions of clean and air-exposed metallic gold (assuming ferrocene/ferrocenium oxidation at 4.8 eV).

charge transport are summarized in **Table 3**. A close examination of Table 2 shows that despite seeming disparities in crystal system, **P-BTDT**, **Bp-BTDT**, and **Np-BTDT** are structurally quite similar. The crystal lattices and molecular arrangements within the unit cells of **BBTDT** and **PF-BTDT** are discussed separately.

2.3.1. Crystal Structures of P-BTDT, Bp-BTDT, and Np-BTDT

First we note that although **Np-BTDT** crystallizes in a monoclinic lattice, the packing arrangement of the **Np-BTDT** molecules bears striking resemblance to the packing of **P-BTDT** and **Bp-BTDT**, which crystallize in triclinic lattices. For example, the lattice parameter *a* and the lattice parameter *b* for these three **BTDTs** are nearly identical, and the *c* lattice parameters are nearly twice the respective molecular lengths (**Figure 2**). Furthermore, close examination (Supporting Information Table S1–S5) shows that the unit cells of these compounds contain four molecules with the nearest neighbors exhibiting a herringbone packing motif (Figure 2). The local packing parameters, such as interplanar distance, pitch angle, roll angle (defined in Supporting Information Figure S2), and herringbone angle also reflect the similarity between these three **BTDT** crystals and are summarized in Table 3. This packing configuration is similar to that of pentacene[6] and other high mobility acene semiconductors.[5]

2.3.2. Crystal Structures of BBTDT and PF-BTDT

BBTDT crystallizes in a monoclinic lattice (space group $P2_1/a$) with two molecules per unit cell. This structure also exhibits a herringbone packing motif, similar to those observed in **P-BTDT**, **Bp-BTDT**, and **Np-BTDT** above, but has unit cell parameters that are significantly different from those **BTDTs**

Table 2. Crystal system, space group, and lattice parameters for bulk BTDT crystals at T = 298 K.[a] Note that in order to facilitate comparison between the molecules, the derived lattice vectors *a* and *b* for P-BTDT, and Bp-BTDT are exchanged in comparison to the.cif files. Similarly, for BBTDT, the lattice vectors *a* and *c* are exchanged. This does not affect the space group designation for the triclinic lattices. For BBTDT, the exchange of the *a* and *c* axes changes the space group from P 2_1/c to P 2_1/a, but the unique axis *b* remains unchanged.

Compound	Crystal system	Space group	a [Å]	b [Å]	c [Å]	α [°]	β [°]	γ [°]
P-BTDT	Triclinic	$P\bar{1}$	7.73	5.96	31.16	94.40	95.20	90.16
Bp-BTDT	Triclinic	$P\bar{1}$	7.72	5.93	39.35	89.40	86.18	89.87
Np-BTDT[a]	Monoclinic	Pc	7.64	5.90	35.80	90.00	95.23	90.00
BBTDT	Monoclinic	$P2_1/a$	11.35	3.94	21.89	90.00	104.00	90.00
PF-BTDT	Monoclinic	$P2_1/c$	8.18	6.21	29.04	90.00	93.31	90.00

[a]Single crystal diffraction measurement of **Np-BTDT** was performed only at T = 100 K. At room temperature, the Np-BTDT crystals did not diffract to sufficient resolution required for successful determination of the single crystal structure. The listed values are obtained by using the lattice parameters obtained at T = 100 K, and by assuming that the thermal expansion coefficients for **Np-BTDT** single crystals are equal to the average of the thermal expansion coefficients of **P-BTDT**, **Bp-BTDT**, **PF-BTDT**, and **BBTDT**, for which the measurements were performed at both T = 100 K and T = 298 K.

Table 3. Local packing parameters based on single crystal diffraction. Slight deviations from the expected symmetries (see Supporting Information) are due to approximations in the determination of herringbone, pitch, and roll angles of the BTDT molecules.

Compound	Packing	Herringbone Angle[a] [°]	Interplanar Angle[b] [°]	Roll Angle [°]	Pitch Angle [°]	Interplanar Distance[c] [Å]	S-S Distance [Å]	Density [g/cm^3]
P-BTDT	Herringbone	49.5	8	65.0	0	2.48	3.71	1.502
Bp-BTDT	Herringbone	49.8	9	64.5	0	2.48	3.69	1.472
Np-BTDT	Herringbone	49.1	3	63.5	0	2.44	3.62	1.540
BBTDT	Herringbone	129.0	0	27.0	0	3.55	3.60	1.714
PF-BTDT	Herringbone	135.6	3	21.5	8.5	3.49	3.64	1.859

[a]The herringbone angle is defined as the interplanar angle for the diagonally aligned molecules. The molecular planes for these calculations are defined as the planes formed by the sulfur atoms of the BTDT cores; [b]The interplanar angle is defined as the angle between the planes of the BTDT cores and the aryl functional groups within the molecules; [c]The interplanar distance is the normal separation of the parallel molecules that are shifted as compared to an idealized face-to-face π-stack (see Supporting Information Figure S2).

Adv. Funct. Mater. **2013**,
DOI: 10.1002/adfm.201203439

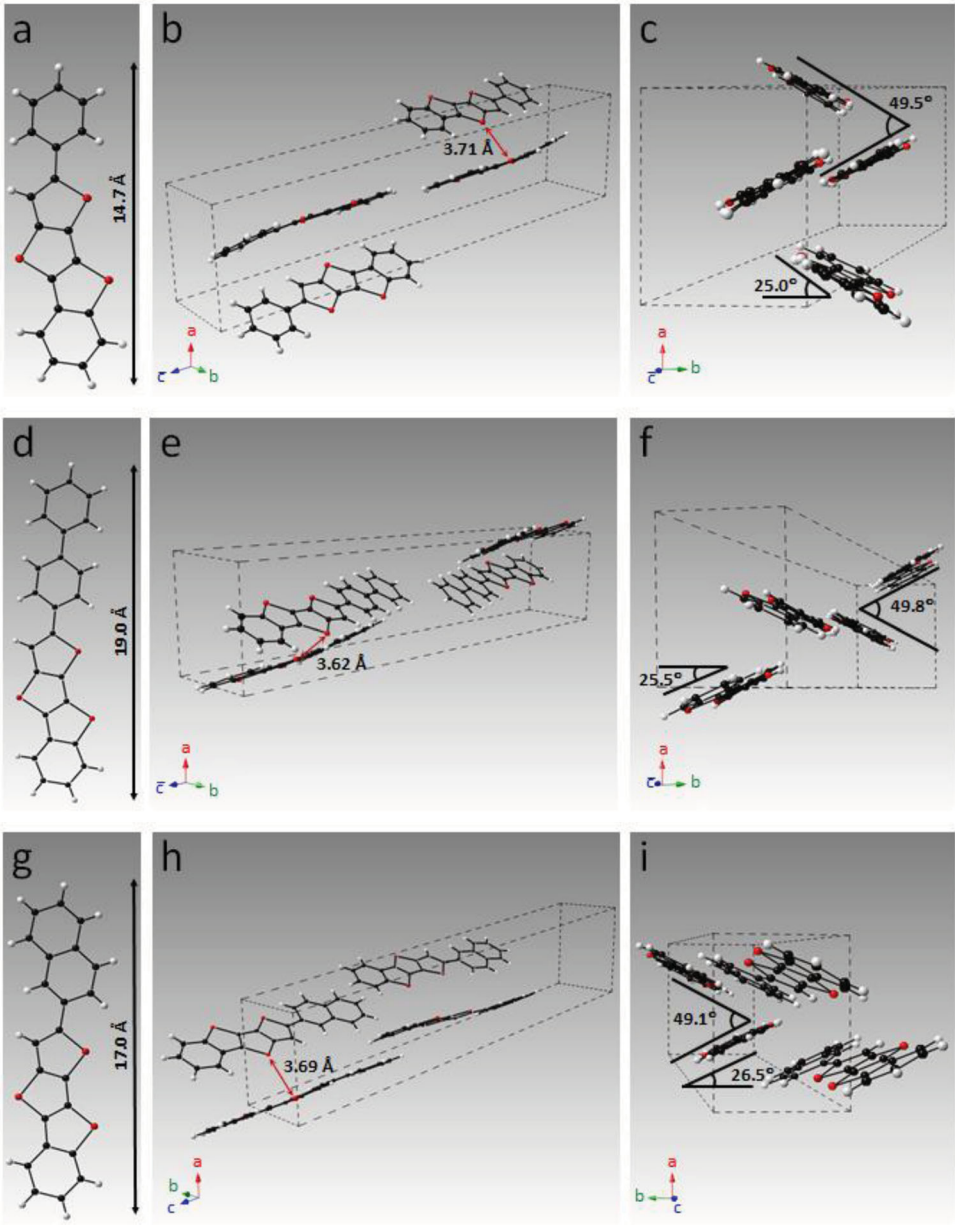

Figure 2. Molecular and crystal structures of **P-BTDT** (a–c), **Bp-BTDT** (d–f), and **Np-BTDT** (g–i) as derived from single-crystal diffraction analysis. All local packing parameters are reported in Table 3. Red, black, and white colors indicate sulfur, carbon, and hydrogen atoms, respectively. Views from near the [11$\bar{1}$] or [1$\bar{1}$1] directions are shown in (b,e,h), and a view nearly parallel to the *c*-axis highlights the herringbone packing of the molecules (c,f,i). Red arrows indicate the closest S-S contact distances, while the herringbone angles and angles between the molecules and the [010] lattice direction (the complement of the roll angle) are shown in (c,f,i).

(Table 2). Furthermore, the interplanar distance for nearest neighbors of 3.55 Å, the roll angle of 27°, and the herringbone angle of ≈129° (**Figure 3**), differ from the corresponding values of 2.44–2.48 Å, ≈64° and ≈49°, respectively, in the **P-BTDT**, **Bp-BTDT**, and **Np-BTDT** crystal structures. These distinctions are relevant because they directly correlate with the degree of π orbital overlap, which in turn governs the efficiency of charge transport between neighboring molecules. Specifically, the interplanar distance and roll angle determine the π orbital interaction between cofacial parallel neighboring molecules, and the herringbone angle determines the degree of interaction between diagonally aligned molecules.

PF-BTDT crystals (Figure 3, Supporting Information Table S5) belong to the same crystal system (monoclinic space group $P2_1/c$) as **BBTDT** (Figure 3, Supporting Information Table S2). However, the separation between the centroids of the molecules that are related by herringbone symmetry is ≈15 Å, which is ≈2.5× that for **BBTDT** (5.9 Å). This

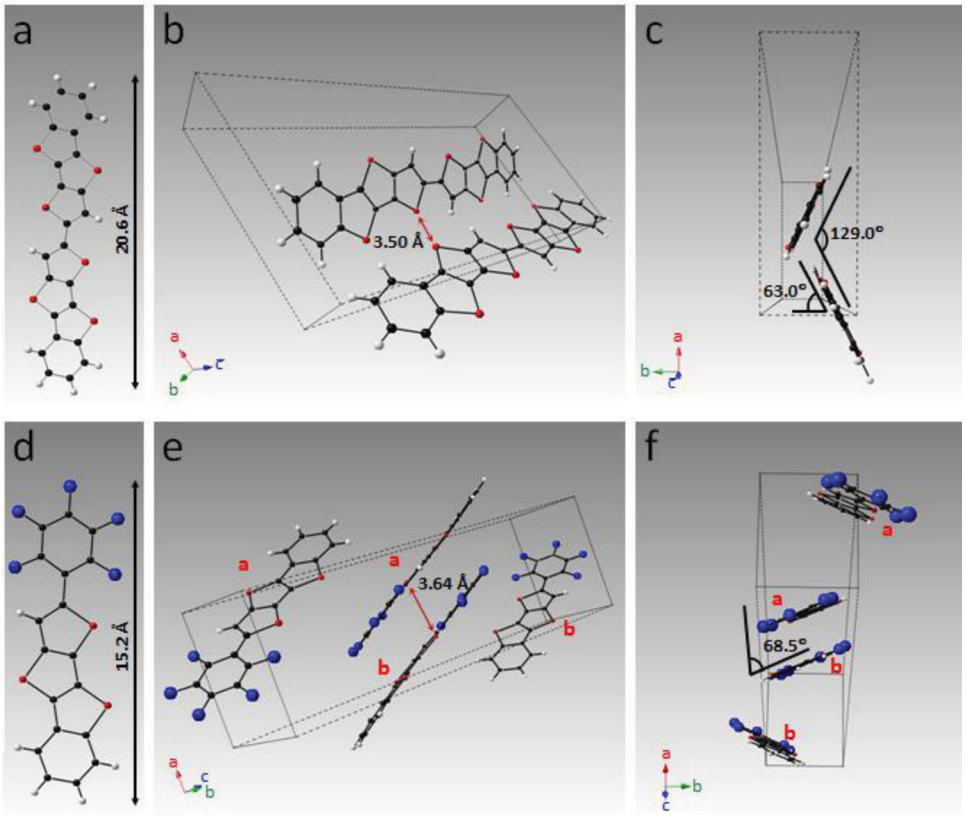

Figure 3. Molecular and crystal structure of **BBTDT** (a–c) and **PF-BTDT** (d–f) as derived from single-crystal diffraction analysis. All local packing parameters are reported in Table 3. Red, black, white, blue colors indicate sulfur, carbon, hydrogen, and fluorine atoms, respectively. For **BBTDT**, a view from near the [11$\bar{1}$] direction is shown in (b) and a view nearly parallel to the *c*-axis highlights the herringbone packing of the molecules (c). Red arrows indicate the closest S-S contact distances, while the derived herringbone angles and angles between the molecules and the [010] lattice direction (the complement of the roll angle) is shown in (c). For **PF-BTDT**, a view from near the [01$\bar{1}$] direction is shown in (e) and a view nearly parallel to the *c*-axis is shown in (f). Nearest-neighbor molecules are co-facially packed at a distance of 3.64 Å. Herringbone symmetry exists between the pair of molecules labeled "a" and the pair labeled "b", but the large separation between these molecules (≈15 Å) effectively eliminates direct charge transport between them.

effectively eliminates any direct charge transport between these molecules. In addition, the nearest-neighbor molecules are co-facially aligned but in an anti-parallel fashion (Figure 3e). This also significantly reduces the π orbital overlap between the co-facially aligned molecules. We will return to these structural distinctions between **BTDTs** when we discuss the thin film structures and TFT electronic performance in the sections which follow.

2.4. GIWAXS Analysis of Semiconductor Thin Films

GIWAXS measurements (Supporting Information Figure S11) were carried out to investigate the effects on the **BTDT** crystal structures induced by confinement in thin films. In an effort to optimize film deposition conditions, three types of substrates, bare Si/SiO_2, HMDS-functionalized Si/SiO_2, and OTS-functionalized Si/SiO_2, were utilized and the effect of the growth temperature was assessed by TFT electrical evaluation (**Table 4**) and out-of-plane X-ray scattering measurements (Supporting Information Figure S3–S10). Finally, OTS-functionalized Si/SiO_2 substrates were chosen for GIWAXS measurements because the best OTFT performance is observed for this surface treatment of the gate dielectric (Table 4). **BTDT** films of nominal 3 nm thickness were chosen because the charge transport in TFTs is generally limited to the first 3–5 nm at the dielectric-semiconductor interface.[21] In addition, GIWAXS measurements were performed only on films deposited with the substrate temperature (T_D) for which maximum TFT performance was observed.

The GIWAXS images (Supporting Information Figure S11) reveal that the scattered intensity is distributed along a series of q_z-extended rods at discrete points on the q_{xy} axis. This implies that the **BTDT** films do not consist of crystallites randomly oriented in 3D, but instead have one of the crystallographic axes at a fixed angle with respect to the surface normal. Furthermore, because all the diffraction peaks are observed, regardless of the azimuthal orientation of the sample with respect to the incident beam, the **BTDT** films likely consist of crystallites that are randomly oriented in-plane (2D powders). The q_{xy} positions of

Adv. Funct. Mater. **2013**,
DOI: 10.1002/adfm.201203439

Table 4. Derived lattice parameters and molecular orientations within the unit cell for **BTDTs** in bulk and thin film form. The tilt angle of the molecules in single crystals is defined as the angle between the direction of the long molecular axis and the normal to the (001) plane.

Molecule	Medium	a [Å]	b [Å]	c [Å]	α [°]	β [°]	γ [°]	Tilt Angle [°]	Herringbone Angle [°]
P-BTDT	Bulk	7.73	5.96	31.06	94.4	95.2	90.2	14.1	46.9
	Thin film[a)]	7.88	6.05	30.88	94.3	96.5	≈90.0	10.9	58.1
	Thin film[b)]	7.88	6.05	31.02	92.5	99.2	≈90.0	12.9	18.9
Bp-BTDT	Bulk	7.72	5.93	39.35	89.4	86.2	89.9	3.8	49.8
	Thin film[a)]	7.85	5.99	38.00	87.4	84.9	≈90.0	12.7	44.2
	Thin film[b)]	7.85	5.99	38.00	86.9	82.5	≈90.0	9.6	19.7
Np-BTDT	Bulk	7.75	5.92	35.91	90.0	95.2	90.0	8.8	49.1
	Thin film[a)]	7.94	6.07	38.00	90.0	94.4	90.0	9.7	44.6
	Thin film[b)]	7.94	6.07	34.50	90.0	96.8	90.0	12.7	84.6
BBTDT	Bulk	11.35	3.94	21.89	90.0	104.0	90.0	4.3	129.0
	Thin film[a)]	11.51	4.00	21.81	90.0	104.3	90.0	18.3	141.9
	Thin film[b)]	11.51	4.00	21.86	90.0	104.0	90.0	13.6	161.8

[a)] Bulk-like; [b)] Best-fit.

the diffraction peaks (**Figure 4**–e) reveal the 2D crystallographic unit cell in the plane of the substrate. The intensity profiles of the (h k q_z) rods are analyzed separately to determine the molecular arrangement within the unit cell in the out-of-plane analysis section.

2.4.1. In-Plane Microstructure Analysis

For **P-BTDT**, **Bp-BTDT**, **Np-BTDT**, and **BBTDT** films, the q_z-projected 1D intensity profiles along the q_{xy} direction (Figure 4a–d) indicate that the positions of the diffraction peaks are close to those expected for the case where the (001) plane corresponding to their 3D lattices is parallel to the substrate surface. In contrast, the **PF-BTDT** thin films display a crystallographic form substantially different from the bulk structure. For this reason, the in-plane lattices for **PF-BTDT** in thin films will be discussed separately. First, we focus on the case of **P-BTDT**, **Bp-BTDT**, **Np-BTDT**, and **BBTDT** films.

While the **P-BTDT**, **Bp-BTDT**, **Np-BTDT**, and **BBTDT** films appear to consist of crystals with the (001) planes parallel to the substrate surface, for each diffraction peak expected for the (001) orientation of the crystals, a doublet is observed (Figure 4a–d and **Figure 5**). Although a slight splitting may be expected for (*hkl*) diffraction peaks that have non-zero h and k because of the non-orthogonality of the a_b and b_b axes (Table 2), this non-orthogonality of the lattice vectors cannot explain the doublets that are observed close to the expected positions for (*h*0*l*) and (0*kl*) reflections (Figure 5). This observation indicates that **P-BTDT**, **Bp-BTDT**, **Np-BTDT**, and **BBTDT** crystallize with two distinct structures when confined to thin films (Figure 4f–i).

It can be shown that for these four **BTDTs**, the positions of all the diffraction peaks can be indexed by assuming a coexistence of two in-plane rectangular lattices which have lattice parameters close to that for the bulk (001) crystal plane (Figure 4f–i). Additionally, the absence of (10*l*) and (01*l*) reflections and the simultaneous observation of the (21*l*) peak in the GIWAXS data (Figure 4, Supporting Information Figure S11) are indicative of herringbone molecular packing with *p2gg* plane group symmetry.[16,24] This is similar to the case for the 3D crystals of **P-BTDT**, **Bp-BTDT**, **Np-BTDT**, and **BBTDT** where the molecular projections onto the (001) plane reveal a herringbone motif.[9] The aforementioned close correspondence between the bulk and the thin film structures suggests that in thin films the **BTDT** molecules form ordered structures with their long molecular axes aligned close to the surface normal, in direct analogy to the molecular arrangement in the single crystals (see the following section on out-of-plane microstructure analysis).

Despite qualitative similarities to the single crystal (001) plane, note that all in-plane thin film lattices are strained. The *A* lattices for **Np-BTDT**, **Bp-BTDT**, and **BBTDT** exhibit a slight decrease in unit cell area, $\Delta A \approx -1\%$ to -2%, when compared to the (001) plane of their single crystal forms, and the *B* lattices for the four **BTDTs** are expanded by $\Delta A \approx 2.7\%$–4% with respect to the single crystal (0 0 1) plane. Intuitively, the coexistence of two lattices suggests a non-uniform film, such that the **BTDTs** close to the dielectric surface crystallize in the relatively highly strained *B* lattice and the **BTDTs** in thicker film regions crystallize in the *A* lattice. However, this explanation is inadequate to explain the observed compressive strain in the *A* lattices of **Bp-BTDT**, **Np-BTDT**, and **BBTDT**. Regardless, it is important to note that lattice strain can play a critical role in the OTFT performance. For example, a recent GIWAXS and electrical characterization study on TIPS-pentacene TFTs showed that a reduction of ≈7% in the π–π stacking distance correlated with a ≈6-fold increase in carrier mobility.[25]

Unlike the other **BTDT**s, **PF-BTDT** exhibits only a single in-plane lattice (Figure 4j) with observed in-plane lattice parameters of a = 7.05 Å, b = 6.78 Å, and γ = 98.7°. Because the

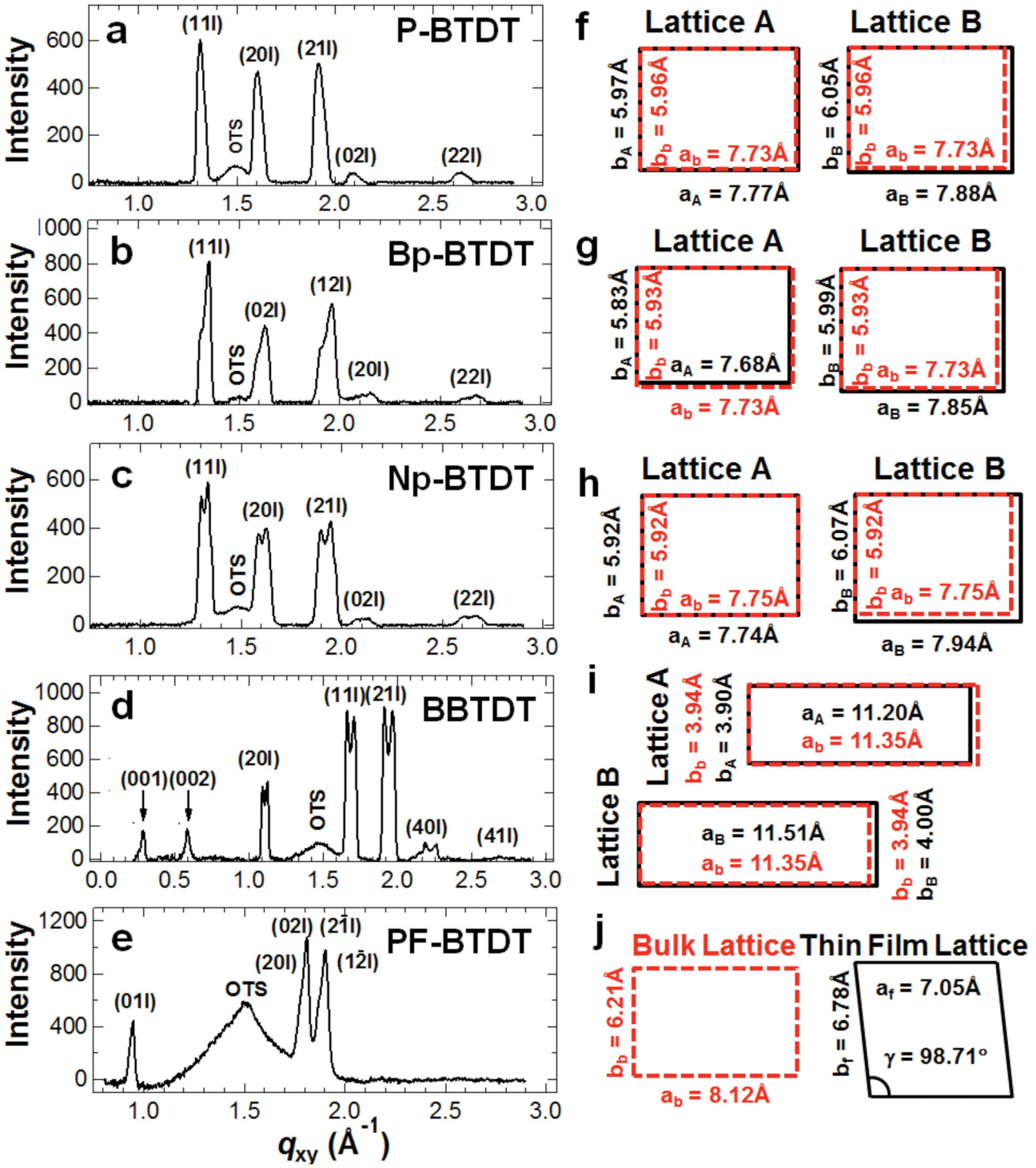

Figure 4. q_z-projected 1D intensity profile as a function of q_{xy} for 3 nm **P-BTDT** (a), **Bp-BTDT** (b), **Np-BTDT** (c), **BBTDT** (d), and **PF-BTDT**(e) films on Si/SiO_2/OTS. For each, the diffraction peak at $q_{xy} \approx 1.5$ Å^{-1} is due to the packing of the OTS alkyl tails in a 2D hexagonal lattice. All other diffraction features originate from the crystalline packing of semiconductor molecules. For **BBTDT** (d), the relatively weak diffraction peaks indicated with the arrows at $q_{xy} \approx 0.295$ and ≈ 0.595 Å^{-1} correspond to diffraction from the (001) and (002) bulk crystal planes, indicating a small fraction of molecules that are oriented with their long molecular axis parallel to the substrate surface. The derived 2D unit cell parameters for **P-BTDT** (f), **Bp-BTDT** (g), **Np-BTDT** (h), **BBTDT** (i), and **PF-BTDT**(j) are shown on the right for the bulk single crystal (red dashed polygon) and thin film (solid black polygon) lattices that comprise the thin film structure. In (f–i) the differences between the observed lattices and the *a*–*b* plane corresponding to the bulk single crystal structures have been exaggerated by 2.5×.

Adv. Funct. Mater. **2013**,
DOI: 10.1002/adfm.201203439

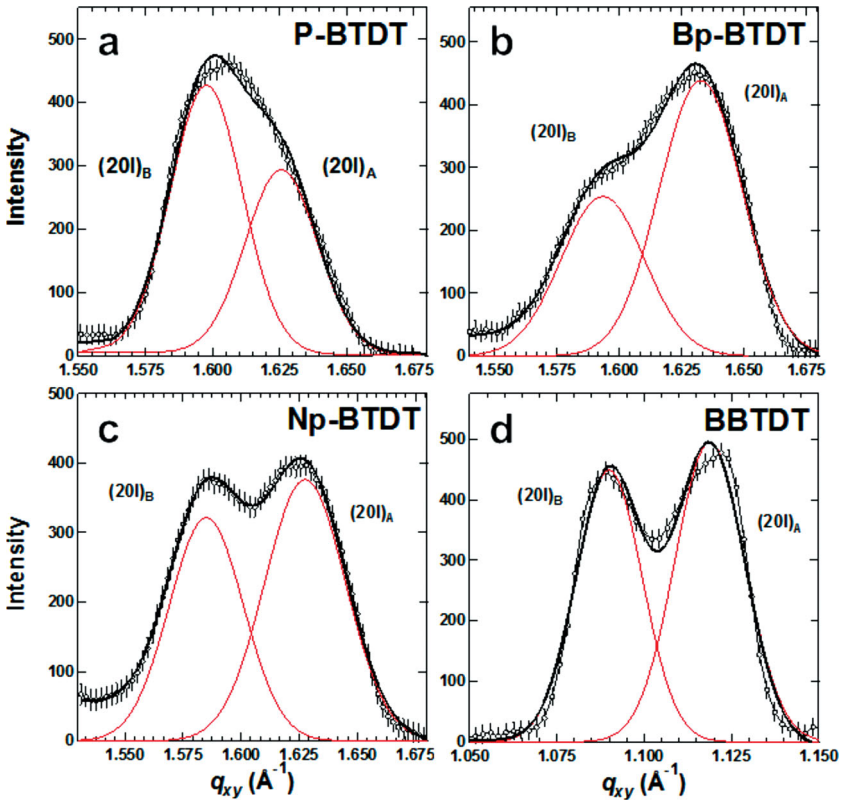

Figure 5. Splitting of the (20*l*) diffraction peak for **P-BTDT**, **Bp-BTDT**, **Np-BTDT**, and **BBTDT**. The peaks indexed as $(20l)_A$ and $(20l)_B$ are from the slightly strained (Lattice *A*) and the highly strained (Lattice *B*) structures. The constituent components of the doublets are shown in red and the sum of the two components is in black.

in-plane lattice was derived from indexing only the four clearly visible diffraction peaks, the validity of the assignment was also examined by measuring 50 nm films deposited at the same temperature and flux (data not shown). The 50 nm films show 10 diffraction peaks corresponding to an in-plane lattice with parameters; $a = 7.24$Å, $b = 6.93$ Å, and $\gamma = 99.6°$. Although the lattice for the 50 nm films is expanded ($\Delta A \approx 4.7\%$) versus the 2D lattice of the 3nm films, it is also an oblique lattice with nearly the same angle γ. This observation clearly demonstrates that unlike the other **BTDTs**, the in-plane lattice for **PF-BTDT** does not correspond to the (001) plane of the single crystal, which for **PF-BTDT** is defined by $a_b = 8.12$ Å, $b_b = 6.21$ Å, and $\gamma = 90°$.

In order to assess the molecular orientation of the **PF-BTDT** molecules within the unit cells, out-of-plane XRD measurements were performed on 50 nm thick films (Supporting Information Figure S6). The XRD plots reveal an interlayer spacing along the interface normal of 16.1 Å, which is comparable to the expected length $L = 15.2$ Å for **PF-BTDT** along its long molecular axis. This observation implies that the **PF-BTDT** molecules, like other **BTDTs** (see out-of-plane analysis), are oriented with their long axes along the interface normal. If the 3D lattice for thin film structure were identical to that of the **PF-BTDT** single crystals, the crystallographic plane $(3\bar{1}20)$ would be parallel to the substrate surface for the case of vertically standing-up molecules (Supporting Information Figure S12). Because the 2D basis for the $(3\bar{1}20)$ plane ($a = 6.82$ Å, $b = 6.38$ Å, and $\gamma = 28.4°$) is substantially different from the observed in-plane lattice for **PF-BTDT** thin films, the thin film structure has no apparent correspondence to any of the crystallographic planes of the bulk lattice. The lack of similarity between the thin film and the single crystal lattices likely arises because, for the dense molecular packing in single crystals, the neighboring **PF-BTDTs** are anti-parallel with their fluoro-aryl groups aligned in opposite directions. It is possible that in thin films the nearest-neighbor **PF-BTDT** molecules are parallel due to the preferential affinity of the fluoro-aryl groups to either the substrate/film or, more likely, the film/air interface. This observation may also explain the apparent expansion of the thin film in-plane unit cell as compared to 2D unit cells for single crystal (001) and $(3\bar{1}20)$ lattice planes.

2.4.2. Out-of-plane Microstructure Analysis

In order to gain further insights into the packing of **BTDTs** in thin films, we extract the lattice parameter *c*, the crystallographic angles α and β, and the orientation of molecules within the unit cell, by analyzing the intensity profile along (h k q_z) rods under a simplified model for the molecular shapes (Supporting Information Figure S13). Briefly, **BTDT** molecules are treated as paralellopipeds of uniform electron density and dimensions $5.5 \times 2.1 \times L$ Å^3, where L is the length of the molecule along the long molecular axis (Figure 2,3), 5.5 Å represents the approximate length along the short molecular axis, and 2.1 Å is roughly the diameter of the sulfur atom. The centroids of the molecules were fixed at the same fractional coordinates as those in the single crystals. The molecule is allowed to rotate about the three orthogonal axes passing through the center of mass. In this model, the symmetry equivalent molecules in the single crystal forms are constrained to rotate by the same amounts. The films are modeled to consist of regions that are 1, 2 or 3 unit cells thick because the **BTDT** films are expected to have regions of varying thicknesses (**Figure 7**). The mathematical formalism is described in the Experimental Section. Fits are performed only for *B* lattices for **P-BTDT**, **Bp-BTDT**, **Np-BTDT**, and **BBTDT** because the intensity profile along the rods for *A* lattices is qualitatively similar to those for *B* lattices. Further analysis of **PF-BTDT** was not performed because the simplfied model gives equally satisfactory mulitple solutions that correspond to disparate molecular arrangements (for example, see **Figure 6**), making it impossible to identify the true molecular packing in the absence of a single crystal reference (Figure 6). For the case of **PF-BTDT**, we do not have such a basis because in thin film form the molecular packing is distinctively different from that in the bulk (Figure 4j). The

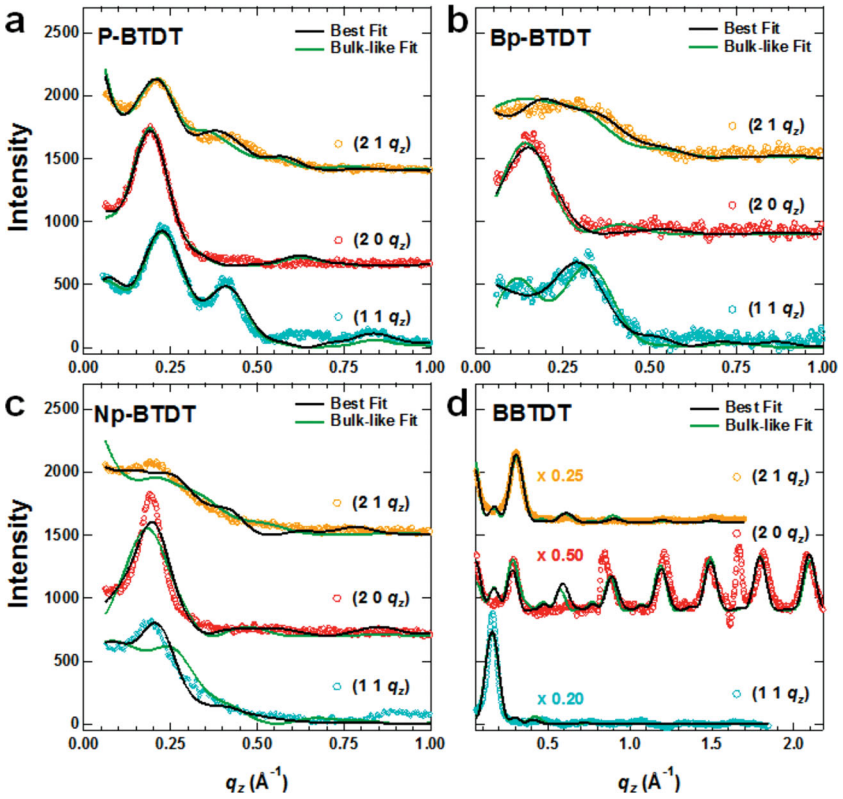

Figure 6. Intensity distribution along the three (h k q_z) rods along with model fits for **P-BTDT** (a), **Bp-BTDT** (b), **Np-BTDT** (c), and **BBTDT** (d). The ($20q_z$) and ($21q_z$) rods are offset for clarity. Note that for BBTDT the sharp intensity modulations at $q_z \approx 0.85$ Å^{-1} and 1.7 Å^{-1} observed along the ($20q_z$) rod arise from reflections from a minority of large crystals oriented along an axis other than (001). These reflections can be seen to be extraneous to the ($20q_z$) rod in Figure 4d.

simultaneous fits for the ($11q_z$), ($20q_z$) and ($21q_z$) rods correponding to the B lattices of **P-BTDT**, **Bp-BTDT**, **Np-BTDT**, and **BBTDT** are shown in Figure 6, and simulation results are summarized in Table 4.

For each **BTDT** derivative, the three data sets were fit simultaneously with the same set of parameters (except for the scaling parameters, see Supporting Information). For **P-BTDT**, **Np-BTDT**, **Bp-BTDT** as well as **BBTDT**, satisfactory fits were achieved under two conditions: when the herringbone angle was constrained to be near a bulk-like value, and when it was far from it (Table 4). For **P-BTDT**, **Bp-BTDT**, and **Np-BTDT**, the three scaling factors for the bulk-like fits were nearly identical, however, for the best fits they differed by more than an order of magnitude. In contrast, for **BBTDT**, the scaling factor for the ($20q_z$) rod was an order of magnitude greater than those for the ($11q_z$) and ($21q_z$) rods for both the bulk-like and the best fits. Physically, the scaling parameters are related to the number of unit cells or the crystal dimensions in the (110), (200), and (210) directions. For the case of **BBTDT**, AFM images (Figure 7d) show that the films consist of elongated crystals/polycrystalline aggregates. Based on the above analysis of the rod profiles, we suggest that the **BBTDT** crystals grow and/or aggregate preferentially along (200) direction in the substrate plane. For the case of **P-BTDT**, **Bp-BTDT**, and

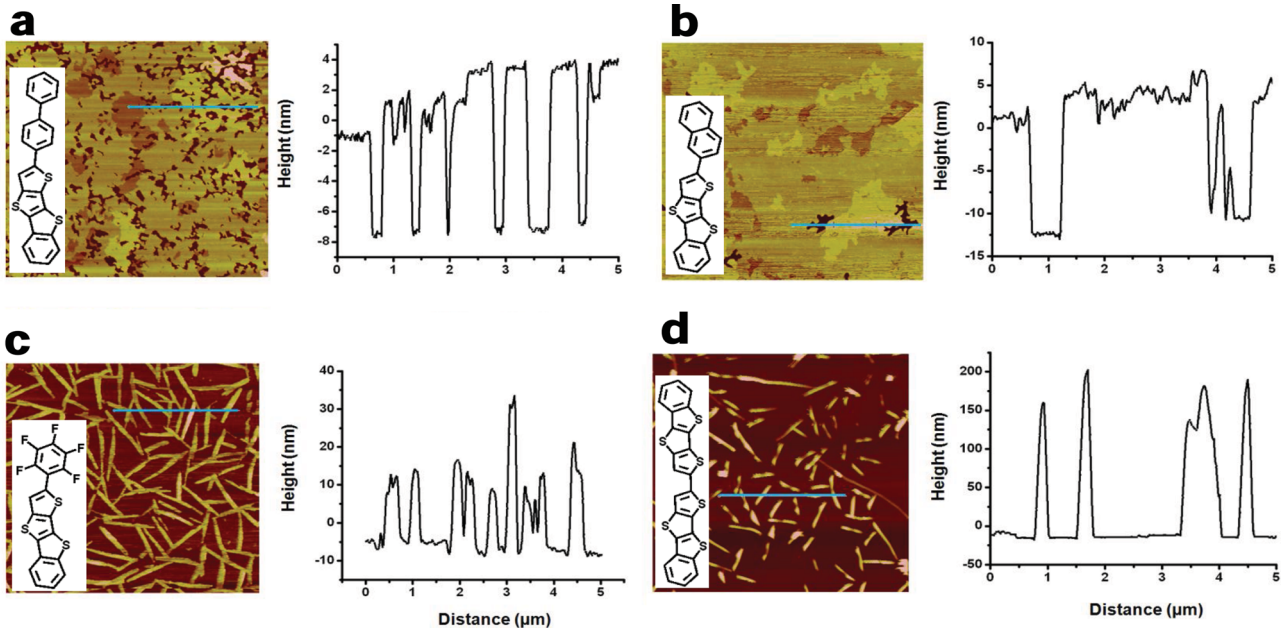

Figure 7. Sub-monolayer (3 nm) film morphologies of **BTDT** films on the Si/SiO_2/OTS substrates. a) **Bp-BTDT** grown at 80 °C, b) **Np-BTDT** grown at 80 °C, c) **PF-BTDT** grown at 40 °C, and d) **BBTDT** grown at 110 °C (tapping mode, topography, 10 μm × 10 μm).

Adv. Funct. Mater. **2013**,
DOI: 10.1002/adfm.201203439

Np-BTDT, no such preferential growth direction is observable in the AFM images (Figure 7a,b), which show nearly uniform film morphologies, and also in the GIWAXS measurements (Figure 4, Supporting Information Figure S11), which show that the coherence lengths along the (110), (200) and (210) are very similar. These observations suggest that for **P-BTDT**, **Bp-BTDT**, and **Np-BTDT**, the bulk-like fits obtained with similar scaling factors for the three rod profiles likely represent the correct molecular arrangements within the unit cell. For these **BTDTs**, the best fit and the bulk-like fit are qualitatively equally good representations of the rod profiles. Therefore, it seems reasonable to suggest that the molecular arrangements in all the four **BTDT**s are very similar to those in their single crystal forms.

Visual inspection of the intensity profiles along the (h k q_z) rods suggests that all **BTDT** films are more than one unit cell thick, especially **BBTDT** films, where the ($20q_z$) rod exhibits strong intensity modulations which extend up to at least $q_z \approx 2.3$ Å^{-1}. Indeed, analysis of the rod profiles reveals that for **BBTDT**, ≈50% of the film is 3 unit cells (u.c.) thick, and 30% is 2 unit cells thick. In contrast, only 20% of the **P-BTDT** film is 2 unit cells thick. For **Bp-BTDT** and **Np-BTDT** (Figure 6), the (h k q_z) rods are relatively featureless. For these cases, fits to the data reveal that more than ≈90% of the film is 1 unit cell thick. These observations are qualitatively consistent with the AFM measurements on 3 nm **BTDT** films (Figure 7), where for **BBTDT**, a non-uniform film composed of vertically extended aggregates is observed while highly uniform coverage is observed for the **Bp-BTDT** and **Np-BTDT** films. Note that the fit values for the fractional coverage by films of different thicknesses are robust, and do not vary by more than 5% upon changes in simulation starting conditions. For **P-BTDT**, **Np-BTDT**, **Bp-BTDT**, and **BBTDT**, the fit values of lattice constant c, the crystallographic angles α and β, and the extracted tilts of the molecules with respect to the surface normal (Table 4) are also very robust and reveal that the lattice parameter c and the angles α and β are very close to their single crystal values. Finally, for all four **BTDT**s, the molecules were found to align with their long axes within a tilt of ≈10–20° from the surface normal.

2.5. Organic Thin-Film Transistor (OTFT) Characterization

Thin-film **BTDT** transistors were fabricated in bottom gate-top contact configurations. Highly doped p-type (100) silicon wafers were used as gate electrodes as well as substrates, and 300 nm thermally grown SiO_2 on the Si was used as the gate insulator. The organic semiconductor thin films (50 nm) were vapor-deposited onto the Si/SiO_2, HMDS-treated Si/SiO_2, OTS-treated Si/SiO_2 substrates. Next, 50 nm gold source and drain electrodes were vapor-deposited at 2×10^{-6} Torr through a shadow mask in a high vacuum growth chamber. Devices were fabricated with two sets of device configurations, either with a channel length of 50 μm and a channel width of 2000 μm, or a channel length of 100 μm and channel width of 5000 μm. Current–voltage (I–V) transfer and output plots were measured for each device in air. Key device performance parameters, such as field-effect mobility (μ), threshold voltage (V_T), and on-to-off current ratio (I_{on}/I_{off}), were extracted using standard procedures.[26] The results are summarized in **Table 5**, and representative I–V plots are presented in **Figure 8** and Supporting Information Figure S14.

In general, the **P-BTDT**, **Bp-BTDT**, **Np-BTDT**, and **BBTDT** films exhibit good charge transport characteristics: **Bp-BTDT** (μ = 0.11 cm^2 V^{-1} s^{-1}, max), **BBTDT** (μ = 0.15 cm^2 V^{-1} s^{-1}, max), **Np-BTDT** (μ = 0.079 cm^2 V^{-1} s^{-1}, max), and previously reported **P-BTDT** devices also exhibit excellent performance, μ = 0.70 cm^2 V^{-1} s^{-1}, on OTS substrates at an elevated growth temperature, T_D = 40 °C. In marked contrast to these results, **PF-BTDT** exhibits considerably lower device performance (μ = 6.2×10^{-6} cm^2 V^{-1} s^{-1}, max) relative to other **BTDT** materials. As will be discussed below, these differences in device performance are convincingly related to the thin film molecular packing structures based on the GIWAXS analysis discussed in the previous section.

3. Discussion

The GIWAXS analyses of the **P-BTDT**, **Bp-BTDT**, **Np-BTDT**, and **BBTDT** thin films reveal that the molecules are arranged in crystalline structures that are similar to, but not identical to, their bulk crystal forms. Note that in the thin films the crystallites do not form 3D powders, but are oriented with the (001) planes parallel to the substrate surface. The (001) plane is a high packing density plane in the single crystal forms of these **BTDT**s. This observation may partially explain the high carrier mobilities observed in **BTDT** TFTs because, all other factors being equal, charge transport efficiency is expected to increase with compressed inter-molecular separation,[27] reflecting enhanced π orbital overlap between neighboring molecules. Furthermore, for the present crystallographic orientations, the molecules are aligned essentially along the substrate normal (Table 5). This edge-on **BTDT** orientation ensures that the direction of π orbital overlap between neighboring molecules is suitably aligned to the source–drain direction of TFT charge flow.

The aforementioned four **BTDT**s have similar bulk and thin film crystal lattices, but there are also subtle differences. Two lattices with slightly different strains relative to the single crystal form are observed in each case. Note that the lattice parameters for the B crystal forms of **P-BTDT**, **Np-BTDT**, and **Bp-BTDT** are very similar, and differ by less than 1%. Therefore, the differences in mobilities observed in their TFTs cannot be explained on the basis of intermolecular separation alone. However, the fractional coverage for the two lattices differs from one **BTDT** to another as shown in Figure 5. For example, Gaussian fits to the ($20l$) diffraction peaks for **P-BTDT** show that the integrated intensity ratio for that reflection from the B crystal to that from the A form, I_B/I_A is ≈2.33. In contrast, for **Bp-BTDT**, **Np-BTDT**, and **BBTDT**, I_B/I_A is 0.64, 0.85, and 0.97, respectively. Recall that the B lattices are more strained than the A lattices. Because the strains are expected to arise from the substrate-molecule interactions, it may be expected that the B crystals comprise the layer closest to the substrate. Therefore, for crystalline films having the same thickness and similar lattice parameters, such as for **P-BTDT**, **Np-BTDT** and **Bp-BTDT**, a higher I_B/I_A likely implies a more uniform first layer, which is possibly related to

Table 5. TFT device performance data for **BTDT**-based semiconductor films.

Compound	T_D [°C]	Substrate	μ_{ave}[a] [$cm^2 V^{-1} s^{-1}$]	μ_{max} [$cm^2 V^{-1} s^{-1}$]	V_T[a] [V]	I_{on}/I_{off}[a]
P-BTDT[b]	25	Bare SiO_2	0.042 ± 0.002	0.044	-20 ± 1	$(2.8 \pm 1.0) \times 10^7$
		HMDS	0.040 ± 0.001	0.041	-23 ± 2	$(1.4 \pm 0.5) \times 10^7$
		OTS	0.069 ± 0.001	0.070	-29 ± 2	$(3.3 \pm 0.6) \times 10^7$
	40	Bare SiO_2	0.021 ± 0.002	0.022	-20 ± 1	$(6.3 \pm 2.0) \times 10^6$
		HMDS	0.049 ± 0.005	0.054	-24 ± 1	$(2.6 \pm 1.0) \times 10^7$
		OTS	0.70 ± 0.02	0.72	-41 ± 1	$(1.2 \pm 0.1) \times 10^8$
PF-BTDT	25	Bare SiO_2	NA[c]	–	–	–
		HMDS	$(5.1 \pm 0.8) \times 10^{-7}$	5.9×10^{-7}	-51 ± 2	14 ± 3
		OTS	$(1.3 \pm 0.1) \times 10^{-6}$	1.4×10^{-6}	-40 ± 1	13 ± 1
	50	Bare SiO_2	NA [c]	–	–	–
		HMDS	$(4.3 \pm 1.6) \times 10^{-6}$	6.2×10^{-6}	-65 ± 4	59 ± 35
		OTS	$(7.6 \pm 1.9) \times 10^{-7}$	9.0×10^{-7}	-37 ± 4	11 ± 2
Bp-BTDT	25	Bare SiO_2	0.0034 ± 0.0006	0.0042	-35 ± 3	$(4.5 \pm 0.1) \times 10^5$
		HMDS	0.0077 ± 0.0004	0.0081	-33 ± 1	$(2.7 \pm 0.8) \times 10^6$
		OTS	$(5.3 \pm 1.8) \times 10^{-4}$	7.2×10^{-4}	-37 ± 4	$(1.2 \pm 0.1) \times 10^5$
	80	Bare SiO_2	0.0062 ± 0.0009	0.0068	-13 ± 1	$(7.7 \pm 0.1) \times 10^5$
		HMDS	0.013 ± 0.001	0.014	-13 ± 2	$(1.5 \pm 1.4) \times 10^6$
		OTS	0.11 ± 0.01	0.11	-16 ± 3	$(3.1 \pm 3.8) \times 10^6$
Np-BTDT	25	Bare SiO_2	0.011 ± 0.001	0.011	-15 ± 2	$(5.8 \pm 2.2) \times 10^6$
		HMDS	0.015 ± 0.001	0.015	-24 ± 2	$(9.8 \pm 3.3) \times 10^6$
		OTS	0.054 ± 0.008	0.062	-38 ± 6	$(8.3 \pm 1.8) \times 10^7$
	80	Bare SiO_2	$(2.9 \pm 0.1) \times 10^{-4}$	2.9×10^{-4}	-26 ± 1	$(2.7 \pm 0.1) \times 10^4$
		HMDS	0.074 ± 0.024	0.088	-17 ± 2	$(4.5 \pm 2.6) \times 10^6$
		OTS	0.072 ± 0.008	0.079	-15 ± 7	$(8.6 \pm 5.1) \times 10^7$
BBTDT	25	Bare SiO_2	0.017 ± 0.002	0.018	-3 ± 1	$(7.0 \pm 3.0) \times 10^3$
		HMDS	0.021 ± 0.003	0.023	-10 ± 2	$(5.1 \pm 0.2) \times 10^4$
		OTS	0.041 ± 0.004	0.044	-18 ± 4	$(1.3 \pm 0.6) \times 10^5$
	80	Bare SiO_2	0.026 ± 0.004	0.028	-4 ± 1	$(1.5 \pm 0.4) \times 10^3$
		HMDS	0.073 ± 0.012	0.084	-9 ± 1	$(1.6 \pm 1.0) \times 10^5$
		OTS	0.071 ± 0.014	0.088	-13 ± 4	$(3.1 \pm 0.1) \times 10^6$
	110	Bare SiO_2	0.044 ± 0.010	0.051	-6 ± 1	$(9.3 \pm 7.5) \times 10^2$
		HMDS	0.040 ± 0.023	0.072	-9 ± 1	$(4.0 \pm 3.1) \times 10^4$
		OTS	0.13 ± 0.02	0.15	-9 ± 1	$(2.7 \pm 2.3) \times 10^6$

[a]Average mobilities are obtained for at least 5 devices; [b]The values for P-BTDT are from ref. [9a]; [c]Not active.

the higher mobility observed for **P-BTDT** versus **Np-BTDT** and **Bp-BTDT** (Table 4).

Note here that while the Bragg rod line shape analysis for **Bp-BTDT** and **Np-BTDT** indicates that the films are largely one unit cell thick, meaning that the *A* and the *B* lattices should coexist within the same layer, the AFM images (Figure 7) show that the films are more inhomogenous than that. Therefore, the intuitive scenario, in which the degree of interaction between the semiconducting molecules and the substrate gives rise to distinct strain states of the *A* and the *B* lattices, may still be valid. However, the exact origin of these differences between the X-ray trends and the AFM-derived film topography is not immediately obvious, and a possible extension of the current work would be to examine the relative abundance of the *A* and the *B* lattices as a function of film thickness.

BBTDT differs from **P-BTDT**, **Np-BTDT**, and **Bp-BTDT** with respect to film uniformity. For a nominal film thickness of 3 nm (≈1.5 unit cells), analysis of the (hkq_z) intensity profiles (Figure 6C) show that the dominant **BBTDT** component is 3 unit cells thick, implying inhomogeneous films comprised of vertically extended aggregates separated by empty spaces. This interpretation is qualitatively confirmed by the AFM

Adv. Funct. Mater. **2013**,
DOI: 10.1002/adfm.201203439

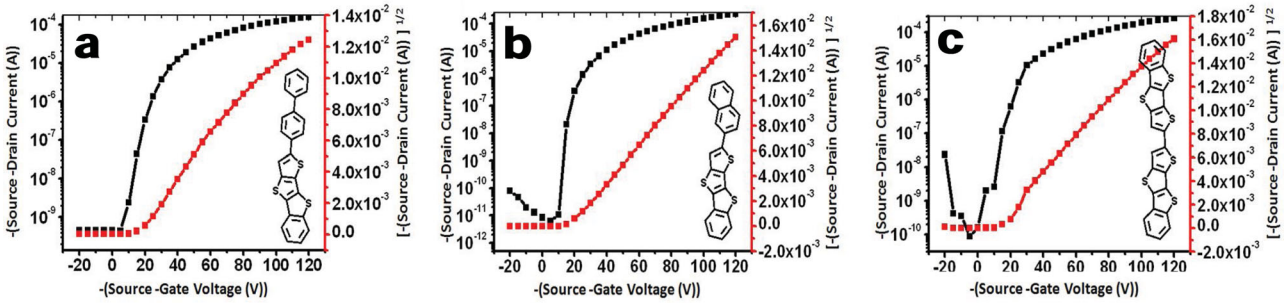

Figure 8. Representative transfer plots for OTFTs fabricated from **Bp-BTDT**, **Np-BTDT**, and **BBTDT** films grown on OTS-coated substrates: a) **Bp-BTDT**, transfer plot; p-type, $\mu = 0.11$ cm^2 V^{-1} s^{-1}, $V_T = -18$ V, and $I_{on}/I_{off} = 3.5 \times 10^5$ in air. Substrate temperature = 80 °C, channel length = 50 μm, and channel width = 2000 μm. b) **Np-BTDT**, transfer plot; p-type, $\mu = 0.079$ cm^2 V^{-1} s^{-1}, $V_T = -18$ V, and $I_{on}/I_{off} = 3.7 \times 10^7$ in air. Substrate temperature = 80 °C, channel length = 100 μm, and channel width = 5000 μm. c) **BBTDT**, transfer plot; p-type, $\mu = 0.15$ cm^2 V^{-1} s^{-1}, $V_T = -9$ V, and $I_{on}/I_{off} = 3.0 \times 10^6$ in air. Substrate temperature = 110 °C, channel length = 50 μm, and channel width = 2000 μm.

data (Figure 7), thereby suggesting a plausible reason for the reduced carrier mobility observed for **BBTDT** versus **P-BTDT**, despite the fact that the larger **BBTDT** π-core relative to the other **BTDT** molecules is expected, all other things being equal, to increase the electronic interaction between π orbitals of adjacent molecules,[22] and to decrease the Marcus reorganization energy.[27,28]

The case of **PF-BTDT** is unique in that the thin film structure does not correlate with the bulk single crystal structure. Nevertheless, note that the unit cell area for the surface-projected **PF-BTDT** lattice differs by only 4% in comparison to the (001) crystallographic plane of the single crystal. Furthermore, in thin films, out-of-plane XRD measurements show that the **PF-BTDT** molecules are aligned with their long molecular axes along surface normal. If the local molecular packing of **PF-BTDT** were identical to that in the single crystal, there would be little interaction between the π orbitals of adjacent molecules because the adjacent molecules are aligned in an anti-parallel orientation about their long molecular axes in the single crystal. Although the **PF-BTDT** molecular packing in thin films does not adhere to the packing structure of the single crystal form, note that the GIWAXS measurements highlight the poor crystallinity of the **PF-BTDT** films. Specifically, for 3 nm films, the most intense reflections from **PF-BTDT** are only twice as strong as the OTS peak (Figure 4e). In marked contrast, the strong reflections from the other BTDT films are ≈5× more intense than those from the underlying OTS SAM. Furthermore, **PF-BTDT** forms vertically extended aggregates as in the case of **BBTDT** (Figure 7c), which reduces the surface coverage of these relatively thick films in the charge transport layer. Taken together, the above factors convincingly explain why the **PF-BTDT** films yield the poorest performing OTFTs.

Other than packing parameters within crystalline domains, the film growth conditions also impact device performance (Table 5). **BTDT** films exhibit enhanced charge carrier mobility as the growth temperature (T_D) is increased. Among the present materials, **Bp-BTDT** and **BBTDT** exhibit the most dramatic changes in mobility. The mobility of **Bp-BTDT**-based OTFTs increases from 7.2×10^{-4} cm^2 V^{-1} s^{-1} (max) at $T_D = 25$ °C to 0.11 cm^2 V^{-1} s^{-1} (max) at $T_D = 80$ °C, and the mobility of the **BBTDT**-based devices increases from 0.044 cm^2 V^{-1} s^{-1} (max) at $T_D = 25$ °C to 0.15 cm^2 V^{-1} s^{-1} at $T_D = 110$ °C on OTS substrates. These trends are in excellent accord with the out-of-plane X-ray diffraction data on the 50 nm thick semiconductor films (Supporting Information Figure S3,S9). As described in the TFT performance summary in Table 5, the enhancement in film crystallinity is best reflected in the results for **Bp-BTDT** and **BBTDT**. In both the cases, the intensity of crystalline reflections increases and the peaks become sharper as the film growth temperature increases from 25 °C to 80 °C to 110 °C (Supporting Information Figure S3,S9), implying that the size and population density of crystalline domains increases in films deposited on hotter substrates. Notably, the **Bp-BTDT** films on OTS substrates strongly exhibit this trend in the sense that not only the peak intensities increase but also a number of new peaks appear in the samples grown at 80 °C relative to 25 °C (Supporting Information Figure S4). Compared with the other molecules, **PF-BTDT** films exhibit less obvious growth condition-mobility trends. In fact, the intensity of crystalline peaks for films grown at 50 °C is somewhat less than for those grown at 25 °C (Supporting Information Figure S5). This crystallinity increase is marked given the grain size growth in the 50 nm thick semiconductor films (Supporting Information Figure S15–S18).

As suggested in the thermal and photo-oxidation evaluations of these materials, the present **BTDT** semiconductors exhibit excellent environmental stability in TFT performance. After two months of shelf-life testing, the **Bp-BTDT** devices fabricated on OTS substrates at 80 °C retain device performance with $\mu = 0.16$ cm^2 V^{-1} s^{-1} (max) and $I_{on}/I_{off} = 6.4 \times 10^4$. In the case of **BBTDT**, the devices fabricated on OTS substrates at 110 °C exhibit $\mu = 0.17$ cm^2 V^{-1} s^{-1} (max) and $I_{on}/I_{off} = 7.5 \times 10^4$ after two months. Previously we showed that **P-BTDT** films exhibit good device performance with $\mu = 0.3$ cm^2 V^{-1} s^{-1} and $I_{on}/I_{off} = 10^7$ after two months of shelf-life testing.[9] The origin of slightly increased mobilities in the **Bp-BTDT** and **BBTDT** devices may reflect additional charge carriers generated by O_2 diffusion into the films. When an organic TFT is exposed to air or O_2, holes are doped into trap states at the semiconductor–SiO_2 gate dielectric interface because O_2 is electron acceptor. This hole filling of trap states can sometimes lead to higher field-effect mobilities.[29]

4. Conclusions

In this contribution, we report a newly synthesized series of **BTDT** molecules and characterize their thin film microstructures and electronic properties. X-ray studies on the **BTDT** thin film structures in conjunction with single crystal data provide a qualitative understanding of how the structural aspects of the molecular solids influence the charge transport properties in thin-film transistor architecture. In the case of **P-BTDT**, **Bp-BTDT**, **Np-BTDT**, and **BBTDT**, two types of in-plane lattices coexist, and the dominance of a more strained lattice relative to the bulk-like lattice may be associated with the excellent charge transport properties of **P-BTDT** films. On the other hand, poor in-plane crystallinity and surface coverage at the dielectric interfacial layer explain the marginal device performance of **PF-BTDT** films. We believe that this study will serve as a structural guide for the future development of thiophene - based organic semiconductors.

5. Experimental Section

Materials and Methods: All chemicals and solvents were of reagent grade and were obtained from Aldrich, Arco, or TCI Chemical Co. Reaction Solvents (toluene, benzene, ether, and THF) were distilled under nitrogen from sodium/benzophenone ketyl, and halogenated solvents were distilled from CaH_2. ^1H and ^{13}C NMR spectra were recorded on a Bruker 500 or a 300 instrument. Chemical shifts for ^1H and ^{13}C NMR spectra were referenced to solvent signals. Differential scanning calorimetry (DSC) was carried out on a Mettler DSC 822 instrument, calibrated with a pure indium sample at a scan rate of 10 K/min. Thermogravimetric analysis (TGA) was performed on a Perkin Elmer TGA-7 thermal analysis system using dry nitrogen as the carrier gas at a flow rate of 40 mL/min. The UV–Vis absorption and fluorescence spectra were obtained using JASCO V-530 and Hitachi F-4500 spectrometers, respectively, and all spectra were measured in the indicated solvents at room temperature. IR spectra were obtained using a JASCO FT/IR-4100 spectrometer. Differential pulse voltammetry experiments were performed with a CH Instruments model CHI621C Electrochemical Analyzer. All measurements were carried out at the temperature indicated with a conventional three-electrode configuration consisting of a platinum disk working electrode, an auxiliary platinum wire electrode, and a non-aqueous Ag reference electrode. The supporting electrolyte was 0.1 M tetrabutylammonium hexafluorophosphate ($TBAPF_6$) in a specified dry solvent. All potentials reported are referenced to an Fc^+/Fc internal standard (at +0.6 V). Elemental analyses were performed on a Heraeus CHN-O-Rapid elemental analyzer. Mass spectrometric data were obtained with a JMS-700 HRMS instrument. Prime grade silicon wafers (p^+-Si) with ≈300 nm (±5%) thermally grown oxide (from Montco Silicon) were used as device substrates. Benzo[*d,d'*]thieno[3,2-*b*;4,5-*b'*] dithiophene and bisbenzo[d,d']thieno[3,2-b;4,5-b'] dithiophene (BBTDT) were prepared according to the literature.[9]

Synthesis of 2-Biphenylbenzo[d,d']thieno[3,2-b;4,5-b']dithiophene (Bp-BTDT): Under nitrogen and anhydrous conditions at 0 °C, 2.5 M *n*-BuLi (0.49 mL in hexanes, 1.23 mmol) was slowly added to a 20 mL THF solution of BTDT (304 mg, 1.23 mmol) and the mixture was stirred for 40 min. Next, tri-*n*-butyltinchloride (0.38 mL, 1.35 mmol) was added and the mixture was stirred for 30 min at this temperature, then warmed to room temperature and stirred overnight. After simple filtration under nitrogen, THF was removed under vacuum and 30 mL toluene was added. The toluene solution was then transferred to a (4-bromophenyl) benzene(316 mg, 1.35 mmol) and tetrakis(triphenylphosphine) palladium (57mg, 0.05 mmol) toluene (30 mL) solution and was refluxed at 140 °C for 2 days. After cooling back to room tempertaure, the desired solid product was collected by filtration, washed with hexanes and ether, and then purified by gradient sublimation at pressures of ~ 10^{-5} Torr at 270°C, giving a bright-yellow solid, 417 mg; yield, 85%. Mp: 392 °C. This material was insufficiently soluble to obtain a useful ^1H and ^{13}C NMR spectrum. Anal. Calcd for $C_{24}H_{14}S_3$: C, 72.32; H, 3.54; Found: C, 72.25; H, 3.63. HRMS (EI, m/z) calcd.: 398.0254 (M^+). Found: 398.0258. The molecular structure of Bp-BTDT has been confirmed by X-ray diffraction.

Synthesis of 2-Naphthalenebenzo[d,d']thieno[3,2-b;4,5-b']dithiophene (Np-BTDT): Similar to above Bp-BTDT synthetic procedure, 2-bromonaphthalene (279 mg, 1.35 mmol) was used instead of (4-bromophenyl)benzene. After simliar work up, the desired product was purified by gradient sublimation at pressures of ~ 10^{-5} Torr at 260 °C, giving a bright-yellow solid, 376 mg; yield, 82.4%. Mp: 299 °C. ^1H NMR (300 MHz, DMSO-d_6): δ 8.29 (d, J = 6.3 Hz, 1H), 8.23 (s, 1H), 8.12 (d, J = 7.8 Hz, 1H), 7.97 (m, 5H), 7.52 (m, 4H). This material was insufficiently soluble to obtain a useful ^{13}C NMR spectrum. Anal. Calcd for $C_{22}H_{12}S_3$: C, 70.93; H, 3.25;Found: C, 70.81; H, 3.34. HRMS (EI, m/z) calcd.: 372.0101 (M^+). Found: 372.0098.

Synthesis of 2-Pentafluorophenylbenzo[d,d']thieno[3,2-b;4,5-b'] dithiophene (PF-BTDT): Similar to above Bp-BTDT synthetic procedure, bromopentafluorobezene (0.17 mL, 1.36 mmol) was used instead of (4-bromophenyl)benzene. After similar work up, the desired product was purified by gradient sublimation at pressures of ≈10^{-5} Torr at 260 °C, giving a bright-yellow solid, 165 mg; yield, 35%. Mp: 316 °C. ^1H NMR (500 MHz, $CDCl_3$): δ7.89 (d, J = 8.0 Hz, 1H), 7.87 (d, J = 8.0 Hz, 1H), 7.79 (s, 1H), 7.47 (t, J = 8.0 Hz, 1H). 7.40 (t, J = 8.0 Hz, 1H). This material was insufficiently soluble to obtain a useful ^{13}C NMR spectrum.^{19}F NMR (282 MHz, $CDCl_3$): δ -139, -154, -161. Anal. Calcd for $C_{18}H_5F_5S_3$: C, 52.42; H, 1.22; Found: C, 52.35; H, 1.34. HRMS (EI, m/z) calcd.: 411.9474 (M^+). Found: 411.9476.

Single Crystal Structure Determination: Crystals suitable for X-ray diffraction were crystallized from a hot trimethylbenzene solution. Then the single crystals were mounted in oil (Infineum V8512) on a glass fiber under a nitrogen cold stream at 100(2)K or at room temperature. X-Ray diffraction data were collected on Kappa diffractometer, equipped with Cu I μS source and an APEX II CCD detector. Data were collected, integrated and corrected for decay and Lp effects using Bruker APEX II software. Final unit cell parameters were obtained through a refinement of all observed reflections during data integration. A Face-indexed absorption correction was performed via XPREP. The structure was solved and refined using the SHELXTL suite of software. All of the non-hydrogen atoms were refined anisotropically. Hydrogen atoms attached to carbon atoms were fixed at calculated positions and refined using a riding mode. Selected crystallographic information and additional refinement details are provided in Supporting Information Table S2 and S5.

Thin Film Structure Characterization: Grazing incidence wide angle X-ray scattering (GIWAXS) measurements on BTDT thin films were carried out at room temperature at beamline 33BM-C of the Argonne National Laboratory's Advanced Photon Source (APS) using X-rays of wavelength λ = 0.826 Å and a MAR 345 image plate area detector. The incident beam size was 2.0 (h) *x* 0.05 (v) mm^2 and the incident flux was 5×10^{10} photons/s. The out-of-plane XRD data were collected on an in-house 18 kW Rigaku ATXG diffractometer using a multilayer parabolic mirror, NaI scintillation detector and X-rays of wavelength λ = 1.542 Å.

Analysis of Bragg Rod Intensity Profiles: Analysis of the (h k q_z) rods was completed for each BTDT by performing simultaneous fits of background subtracted line profiles of ($11q_z$), ($02q_z$) and ($12q_z$) rods. The intensity along the rod was calculated using $I_{hk}(q_z) = N_{hk}(t_1 + P_2t_2 + P_3(1 - t_1 - t_2))|\sum_i f_i e^{i\vec{q}\cdot\vec{r}_{0i}}|^2$, where t_1, t_2 and t_3 are the fractions of the surface covered by 1, 2 and 3 unit cell thick regions. P_2 and P_3 are the lattice sums over two and three unit cells along the surface normal, specifically, $P_2 = \left|\left(1 - e^{i\,2\vec{q}\cdot\vec{c}}\right)/\left(1 - e^{i\,\vec{q}\cdot\vec{c}}\right)\right|^2$, $P_3 = \left|\left(1 - e^{i\,3\vec{q}\cdot\vec{c}}\right)/\left(1 - e^{i\,\vec{q}\cdot\vec{c}}\right)\right|^2$. The scattering vector $\vec{q}$ is given by $\vec{q} = h\left(\vec{a}^* - a_z^*\right) + k\left(\vec{b}^* - b_z^*\right) + q_z$, where $a_z^*$and b_z^* are the surface normal components of the reciprocal lattice vectors a^* and b^*, and depend upon the crystallographic angles α and β. The form factor f_i of the i^{th} molecule in the unit cell is given by $f_i = \int_V e^{i\,\vec{q}\,\vec{r}_i'} d^3r_i$, where

DOI: 10.1002/adfm.201203439

$(r_i')_j = \sum_l \left(R_x(\eta_1)\, R_y(\eta_2)\, R_z(\eta_3)\right)_{j,l} (r_i)_l$ are the components of the position vector $\vec{r}_i'$ and R_x, R_y and R_z are the conventional rotation matrices. The position of the centroids of the i^{th} molecule is r_{0i} and N_{hk} is a scale factor. Because the simulations span a large parameter space, a number of solutions (local minima) can be obtained depending on the starting values of the fitting parameters. Best-fits were obtained by running the simulations for at least 20 different starting conditions.

OTFT Fabrication: TFTs were fabricated in bottom gate-top contact configuration. Highly doped p-type (100) silicon wafers (<0.004 Ω cm) were used as gate electrodes as well as substrates, and 300 nm SiO_2 thermally grown on Si was used as the gate insulator. The unit area capacitance was taken to be 10 nF cm^{-2}. The substrate surface was treated with octadecatrichlorosilane (OTS) and hexamethyldisilazane (HMDS) purchased from Sigma-Aldrich Chemical Co. A few drops of HMDS were loaded inside a self-assembly chamber under an N_2 blanket. The SiO_2/Si substrates were exposed to this atmosphere for at least 7.0 days to give a hydrophobic surface. After HMDS deposition, the advancing aqueous contact angle is 95°. OTS-modified substrates were fabricated by immersing Si/SiO_2 substrates in 3.0 mM hexane solutions of the silane reagent for 1 hour after leaving the solution in air under 55–60% humidity for 10 h. After OTS deposition, the substrates were sonicated with hexane, acetone, and, ethanol. The contact angle of a water drop on OTS SAM is 104°. Semiconductor thin films (50 nm) were next vapor-deposited onto the Si/SiO_2 held at predetermined temperatures of 25 °C, 80 °C for Bp-BTDT and Np-BTDT, 25 °C, 80 °C, and 110 °C for BBTDT with a deposition rate of 0.3 Å/s at 6×10^{-6} Torr, employing a high-vacuum deposition chamber (Denton Vacuum, Inc., USA). Gold source and drain electrodes (50 nm) were vapor-deposited at 2×10^{-6} Torr through a shadow mask in the vacuum deposition chamber. Devices were fabricated with two sets of device configuration, a channel length of 50 μm and a channel width of 2000 μm as well as a channel length of 100 μm and channel width of 5000 μm.

OTFT Characterization: *I–V* plots of device performance were measured under vacuum, and transfer and output plots were recorded for each device. The *I–V*) characteristics of the devices were measured using a Keithley 6430 subfemtoammeter and a Keithly 2400 source meter, operated by a local Labview program and GPIB communication. Key device parameters, such as charge carrier mobility (μ) and on-to-off current ratio (I_{on}/I_{off}), were extracted from the source-drain current (I_{SD}) versus source-gate voltage (V_{SG}) characteristics employing standard procedures. Mobilities were obtained from the formula defined by the saturation regime in transfer plots, $\mu = 2I_{SD}L/(C_iW(V_{SG} - V_T)^2)$, where I_{SD} is the source-drain current, V_{SG} is source-gate voltage, L is the channel length, W is the channel width, C_i is the capacitance of the gate dielectric, V_T is the threshold voltage. Threshold voltage was obtained from *x* intercept of V_{SG} vs. $I_{SD}^{1/2}$ plots.

Film Morphology Measurements: AFM measurements were performed using a JEOL-Microscope (JEOL Ltd. Japan) and Dimension Icon Scanning Probe Microscope (Veeco, USA) in the tapping mode. Crystallographic data (excluding structure factors) for the structures reported in this paper have been deposited with the Cambridge Crystallographic Data Centre as supplementary publication nos. CCDC 916020-916028. Copies of the data can be obtained free of charge from the CCDC via www.ccdc.cam.ac.uk/data_request/cif.

Supporting information

Supporting Information is available from the Wiley Online Library or from the author.

Acknowledgements

This research, including use of the J.B. Cohen X-ray Diffraction Facility, was supported by the NSF MRSEC program (grant DMR-1121262) at the Materials Research Center of Northwestern U., by AFOSR (grants FA9550-08-1-0331 and FA9550-11-10275), by the National Science Council, Taiwan, Republic of China (grants NSC100-2628-M-008-004, NSC101-2113-M-008-005), and by the Industrial Technology Research Institute of Taiwan (grant B361A51500). Use of the Advanced Photon Source, 33BM-C, was supported by the U.S. DOE, Office of Science, Office of Basic Energy Sciences, under Contract No. DE-AC02-06CH11357.

Received: November 21, 2012
Revised: December 19, 2012
Published online:

[1] a) Y. G. Wen, Y. Q. Liu, Y. L. Guo, G. Yu, W. P. Hu, *Chem. Rev.* **2011**, *111*, 3358; b) M. J. Spijkman, K. Myny, E. C. P. Smits, P. Heremans, P. W. M. Blom, D. M. de Leeuw, *Adv. Mater.* **2011**, *23*, 3231; c) W. Shao, H. L. Dong, L. Jiang, W. P. Hu, *Chem. Sci.* **2011**, *2*, 590; d) X. W. Zhan, A. Facchetti, S. Barlow, T. J. Marks, M. A. Ratner, M. R. Wasielewski, S. R. Marder, *Adv. Mater.* **2011**, *23*, 268; e) A. A. Virkar, S. Mannsfeld, Z. A. Bao, N. Stingelin, *Adv. Mater.* **2010**, *22*, 3857; f) H. Sirringhaus, M. Bird, T. Richards, N. Zhao, *Adv. Mater.* **2010**, *22*, 3893; g) W. H. Lee, J. H. Cho, K. Cho, *J. Mater. Chem.* **2010**, *20*, 2549; h) G. Gelinck, P. Heremans, K. Nomoto, T. D. Anthopoulos, *Adv. Mater.* **2010**, *22*, 3778; i) T. J. Marks, *MRS Bull.* **2010**, *35*, 1018; j) M. E. Roberts, A. N. Sokolov, Z. N. Bao, *J. Mater. Chem.* **2009**, *19*, 3351; k) M. L. Tang, S. C. B. Mannsfeld, Y. S. Sun, H. A. Becerril, Z. N. Bao, *J. Am. Chem. Soc.* **2009**, *131*, 882; l) N. Kobayashi, M. Sasaki, K. Nomoto, *Chem. Mater.* **2009**, *21*, 552; m) M. L. Tang, A. D. Reichardt, N. Miyaki, R. M. Stoltenberg, Z. Bao, *J. Am. Chem. Soc.* **2008**, *130*, 6064; n) S. Subramanian, S. K. Park, S. R. Parkin, V. Podzorov, T. N. Jackson, J. E. Anthony, *J. Am. Chem. Soc.* **2008**, *130*, 2706; o) Y. Didane, G. H. Mehl, A. Kumagai, N. Yoshimoto, C. Videlot-Ackermann, H. Brisset, *J. Am. Chem. Soc.* **2008**, *130*, 17681; p) A. R. Murphy, J. M. J. Frechet, *Chem. Rev.* **2007**, *107*, 1066; q) C. Kim, A. Facchetti, T. J. Marks, *Science* **2007**, *318*, 76; r) B. A. Jones, A. Facchetti, M. R. Wasielewski, T. J. Marks, *J. Am. Chem. Soc.* **2007**, *129*, 15259.

[2] a) H. Yan, Z. H. Chen, Y. Zheng, C. Newman, J. R. Quinn, F. Dotz, M. Kastler, A. Facchetti, *Nature* **2009**, *457*, 679686; b) H. Usta, A. Facchetti*Acc. Chem. Res* **2011**, *44*, 501.

[3] J. E. Anthony, *Chem. Rev.* **2006**, *106*, 5028.

[4] A. C. Arias, J. D. MacKenzie, I. McCulloch, J. Rivnay, A. Salleo, *Chem. Rev.* **2010**, *110*, 3.

[5] a) D. J. Gundlach, J. E. Royer, S. K. Park, S. Subramanian, O. D. Jurchescu, B. H. Hamadani, A. J. Moad, R. J. Kline, L. C. Teague, O. Kirillov, C. A. Richter, J. G. Kushmerick, L. J. Richter, S. R. Parkin, T. N. Jackson, J. E. Anthony, *Nat. Mater.* **2008**, *7*, 216; b) J. M. Choi, J. Lee, D. K. Hwang, J. H. Kim, S. Im, E. Kim, *Appl. Phys. Lett.* **2006**, *88*, 082904; c) C. Santato, I. Manunza, A. Bonfiglio, F. Cicoira, P. Cosseddu, R. Zamboni, M. Muccini, *Appl. Phys. Lett.* **2005**, *86*, 163511; d) J. Reynaert, D. Cheyns, D. Janssen, R. Muller, V. I. Arkhipov, J. Genoe, G. Borghs, P. Heremans, *J. Appl. Phys.* **2005**, *97*, 061301; e) Q. Miao, M. Lefenfeld, T. Q. Nguyen, T. Siegrist, C. Kloc, C. Nuckolls, *Adv. Mater.* **2005**, *17*, 407; f) F. Cicoira, C. Santato, F. Dinelli, M. Murgia, M. A. Loi, F. Biscarini, R. Zamboni, P. Heremans, M. Muccini, *Adv. Funct. Mater.* **2005**, *15*, 375; g) K. Ito, T. Suzuki, Y. Sakamoto, D. Kubota, Y. Inoue, F. Sato, S. Tokito, *Angew. Chem. Int. Ed.* **2003**, *42*, 1159; h) D. J. Gundlach, J. A. Nichols, L. Zhou, T. N. Jackson, *Appl. Phys. Lett.* **2002**, *80*, 2925.

[6] a) C. Kim, P. Y. Huang, J. W. Jhuang, M. C. Chen, J. C. Ho, T. S. Hu, J. Y. Yan, L. H. Chen, G. H. Lee, A. Facchetti, T. J. Marks, *Org. Electron.* **2010**, *11*, 1363; b) Y. N. Li, Y. L. Wu, P. Liu, Z. Prostran, S. Gardner, B. S. Ong, *Chem. Mater.* **2007**, *19*, 418; c) D. H. Kim,

D. Y. Lee, H. S. Lee, W. H. Lee, Y. H. Kim, J. I. Han, K. Cho, *Adv. Mater.* **2007**, *19*, 678.

[7] a) C. R. Swartz, S. R. Parkin, J. E. Bullock, J. E. Anthony, A. C. Mayer, G. G. Malliaras, *Org. Lett.* **2005**, *7*, 3163; b) T. W. Kelley, P. F. Baude, C. Gerlach, D. E. Ender, D. Muyres, M. A. Haase, D. E. Vogel, S. D. Theiss, *Chem. Mater.* **2004**, *16*, 4413; c) H. Meng, M. Bendikov, G. Mitchell, R. Helgeson, F. Wudl, Z. Bao, T. Siegrist, C. Kloc, C. H. Chen, *Adv. Mater.* **2003**, *15*, 1090; d) T. W. Kelley, L. D. Boardman, T. D. Dunbar, D. V. Muyres, M. J. Pellerite, T. Y. P. Smith, *J. Phys. Chem. B* **2003**, *107*, 5877; e) A. R. Volkel, R. A. Street, D. Knipp, *Phys. Rev. B* **2002**, *66*; f) H. Klauk, M. Halik, U. Zschieschang, G. Schmid, W. Radlik, W. Weber, *J. Appl. Phys.* **2002**, *92*, 5259; g) C. D. Dimitrakopoulos, P. R. L. Malenfant, *Adv. Mater.* **2002**, *14*, 99; h) F. Heringdorf, M. C. Reuter, R. M. Tromp, *Nature* **2001**, *412*, 517; i) S. F. Nelson, Y. Y. Lin, D. J. Gundlach, T. N. Jackson, *Appl. Phys. Lett.* **1998**, *72*, 1854; j) D. J. Gundlach, Y. Y. Lin, T. N. Jackson, S. F. Nelson, D. G. Schlom, *IEEE Electron Device Lett.* **1997**, *18*, 87.

[8] a) H. Yamada, Y. Yamashita, M. Kikuchi, H. Watanabe, T. Okujima, H. Uno, T. Ogawa, K. Ohara, N. Ono, *Chem.-Eur. J.* **2005**, *11*, 6212; b) P. Coppo, S. G. Yeates, *Adv. Mater.* **2005**, *17*, 3001; c) A. Maliakal, K. Raghavachari, H. Katz, E. Chandross, T. Siegrist, *Chem. Mater.* **2004**, *16*, 4980.

[9] a) J. Youn, M. C. Chen, Y. J. Liang, H. Huang, R. P. Ortiz, C. Kim, C. Stern, T. S. Hu, L. H. Chen, J. Y. Yan, A. Facchetti, T. J. Marks, *Chem. Mater.* **2010**, *22*, 5031; b) P.-Y. Huang, L.-H. Chen, C. Kim, H.-C. Chang, Y.-J. Liang, C.-Y. Feng, C.-M. Yeh, J.-C. Ho, C.-C. Lee, M.-C. Chen, *ACS Appl. Mater. Interfaces* **2012**, *4*, 6992.

[10] a) Y. Liu, C. A. Di, C. Y. Du, Y. Q. Liu, K. Lu, W. F. Qiu, G. Yu, *Chem.-Eur. J.* **2010**, *16*, 2231; b) C. Kim, M. C. Chen, Y. J. Chiang, Y. J. Guo, J. Youn, H. Huang, Y. J. Liang, Y. J. Lin, Y. W. Huang, T. S. Hu, G. H. Lee, A. Facchetti, T. J. Marks, *Org. Electron.* **2010**, *11*, 801; c) L. Tan, L. Zhang, X. Jiang, X. D. Yang, L. J. Wang, Z. Wang, L. Q. Li, W. P. Hu, Z. G. Shuai, L. Li, D. B. Zhu, *Adv. Funct. Mater.* **2009**, *19*, 272; d) P. Gao, D. Beckmann, H. N. Tsao, X. L. Feng, V. Enkelmann, M. Baumgarten, W. Pisula, K. Mullen, *Adv. Mater.* **2009**, *21*, 213.

[11] S. Shinamura, E. Miyazaki, K. Takimiya, *J. Org. Chem.* **2010**, *75*, 1228; T. Yamamoto, K. Takimiya, *J. Am. Chem. Soc.* **2007**, *129*, 2224.

[12] Y. Liu, Y. Wang, W. P. Wu, Y. Q. Liu, H. X. Xi, L. M. Wang, W. F. Qiu, K. Lu, C. Y. Du, G. Yu, *Adv. Funct. Mater.* **2009**, *19*, 772.

[13] J. H. Gao, R. J. Li, L. Q. Li, Q. Meng, H. Jiang, H. X. Li, W. P. Hu, *Adv. Mater.* **2007**, *19*, 3008.

[14] Y. M. Sun, Y. W. Ma, Y. Q. Liu, Y. Y. Lin, Z. Y. Wang, Y. Wang, C. G. Di, K. Xiao, X. M. Chen, W. F. Qiu, B. Zhang, G. Yu, W. P. Hu, D. B. Zhu, *Adv. Funct. Mater.* **2006**, *16*, 426.

[15] a) S. C. B. Mannsfeld, M. L. Tang, Z. A. Bao, *Adv. Mater.* **2011**, *23*, 127; Y. Quan, S. C. B. Mannsfeld, M. L. Tang, M. Roberts, M. F. Toney, D. M. DeLongchamp, Z. Bao, *Chem. Mater.* **2008**, *20*, 2763; b) T. N. Krauss, E. Barrena, X. N. Zhang, D. G. de Oteyza, J. Major, V. Dehm, F. Wurthner, L. P. Cavalcanti, H. Dosch, *Langmuir* **2008**, *24*, 12742.

[16] S. C. B. Mannsfeld, A. Virkar, C. Reese, M. F. Toney, Z. N. Bao, *Adv. Mater.* **2009**, *21*, 2294.

[17] Q. Yuan, S. C. B. Mannsfeld, M. L. Tang, M. F. Toney, J. Luening, Z. A. Bao, *J. Am. Chem. Soc.* **2008**, *130*, 3502.

[18] a) B. Watts, T. Schuettfort, C. R. McNeill, *Adv. Funct. Mater.* **2011**, *21*, 1122; b) V. Kalihari, E. B. Tadmor, G. Haugstad, C. D. Frisbie, *Adv. Mater.* **2008**, *20*, 4033; c) B. Stadlober, U. Haas, H. Maresch, A. Haase, *Phys. Rev. B* **2006**, *74*, 165302; d) Y. B. Song, C. A. Di, X. D. Yang, S. P. Li, W. Xu, Y. Q. Liu, L. M. Yang, Z. G. Shuai, D. Q. Zhang, D. B. Zhu, *J. Am. Chem. Soc.* **2006**, *128*, 15940; e) H. S. Lee, D. H. Kim, J. H. Cho, Y. D. Park, J. S. Kim, K. Cho, *Adv. Funct. Mater.* **2006**, *16*, 1859; f) S. Pratontep, F. Nuesch, L. Zuppiroli, M. Brinkmann, *Phys. Rev. B* **2005**, *72*, 115101; g) G. Horowitz, *Adv. Funct. Mater.* **2003**, *13*, 53; h) J. W. Orton, M. J. Powell, *Rep. Prog. Phys.* **1980**, *43*, 1263.

[19] a) J. Rivnay, L. H. Jimison, J. E. Northrup, M. F. Toney, R. Noriega, S. F. Lu, T. J. Marks, A. Facchetti, A. Salleo, *Nat. Mater.* **2009**, *8*, 952; b) M. Tello, M. Chiesa, C. M. Duffy, H. Sirringhaus, *Adv. Funct. Mater.* **2008**, *18*, 3907; c) G. E. Pike, C. H. Seager, *J. Appl. Phys.* **1979**, *50*, 3414.

[20] a) U. Zschieschang, F. Ante, M. Schlorholz, M. Schmidt, K. Kern, H. Klauk, *Adv. Mater.* **2010**, *22*, 4489; b) M. Marchl, M. Edler, A. Haase, A. Fian, G. Trimmel, T. Griesser, B. Stadlober, E. Zojer, *Adv. Mater.* **2010**, *22*, 5361; c) K. C. Liao, A. G. Ismail, L. Kreplak, J. Schwartz, I. G. Hill, *Adv. Mater.* **2010**, *22*, 3081; d) U. Kraft, U. Zschieschang, F. Ante, D. Kalblein, C. Kamella, K. Amsharov, M. Jansen, K. Kern, E. Weber, H. Klauk, *J. Mater. Chem.* **2010**, *20*, 6416; e) A. Virkar, S. Mannsfeld, J. H. Oh, M. F. Toney, Y. H. Tan, G. Y. Liu, J. C. Scott, R. Miller, Z. Bao, *Adv. Funct. Mater.* **2009**, *19*, 1962; f) Y. Ito, A. A. Virkar, S. Mannsfeld, J. H. Oh, M. Toney, J. Locklin, Z. A. Bao, *J. Am. Chem. Soc.* **2009**, *131*, 9396; g) S. A. DiBenedetto, A. Facchetti, M. A. Ratner, T. J. Marks, *Adv. Mater.* **2009**, *21*, 1407; h) H. S. Lee, D. H. Kim, J. H. Cho, M. Hwang, Y. Jang, K. Cho, *J. Am. Chem. Soc.* **2008**, *130*, 10556; i) *Organic Field-Effect Transistors*, (Ed: J. L. Zhenan Bao), CRC Press Taylor and Francis Group **2007**; j) H. C. Yang, T. J. Shin, M. M. Ling, K. Cho, C. Y. Ryu, Z. N. Bao, *J. Am. Chem. Soc.* **2005**, *127*, 11542; k) L. L. Chua, J. Zaumseil, J. F. Chang, E. C. W. Ou, P. K. H. Ho, H. Sirringhaus, R. H. Friend, *Nature* **2005**, *434*, 194; l) G. Witte, C. Woll, *J. Mater. Res.* **2004**, *19*, 1889; m) K. P. Pernstich, S. Haas, D. Oberhoff, C. Goldmann, D. J. Gundlach, B. Batlogg, A. N. Rashid, G. Schitter, *J. Appl. Phys.* **2004**, *96*, 6431; n) S. Kobayashi, T. Nishikawa, T. Takenobu, S. Mori, T. Shimoda, T. Mitani, H. Shimotani, N. Yoshimoto, S. Ogawa, Y. Iwasa, *Nat. Mater.* **2004**, *3*, 317; o) *Organic thin-film transistors with field-effect mobility*, Vol. *57*th Annual, 164., (Ed: D. J. N. Gundlach, C.-C. Jackson, T. N. Jackson), Device Research Conference Digest **1999**.

[21] A. Dodabalapur, L. Torsi, H. E. Katz, *Science* **1995**, *268*, 270.

[22] a) J. Youn, P.-Y. Huang, Y.-W. Huang, M.-C. Chen, Y.-J. Lin, H. Huang, R. Ponce Ortiz, C. Stern, M.-C. Chung, C.-Y. Feng, L.-H. Chen, A. Facchetti, T. J. Marks, *Adv. Funct. Mater.* **2012**, *22*, 48; b) M.-C. Chen, Y.-J. Chiang, C. Kim, Y.-J. Guo, S.-Y. Chen, Y.-J. Liang, Y.-W. Huang, T.-S. Hu, G.-H. Lee, A. Facchetti, T. J. Marks, *Chem. Commun.* **2009**, *14*, 1846.

[23] a) S. J. Liu, Q. Zhao, Q. L. Fan, W. Huang, Eur. *J. Inorg. Chem.* **2008**, 2177; J. R. Quinn, F. W. Foss, L. Venkataraman, R. Breslow, *J. Am. Chem. Soc.* **2007**, *129*, 12376; b) F. I. Wu, H. J. Su, C. F. Shu, L. Y. Luo, W. G. Diau, C. H. Cheng, J. P. Duan, G. H. Lee, *J. Mater. Chem.* **2005**, *15*, 1035.

[24] M. K. Durbin, A. G. Richter, C. J. Yu, J. Kmetko, J. M. Bai, P. Dutta, *Phys. Rev. E* **1998**, *58*, 7686.

[25] G. Giri, E. Verploegen, S. C. B. Mannsfeld, S. Atahan-Evrenk, D. H. Kim, S. Y. Lee, H. A. Becerril, A. Aspuru-Guzik, M. F. Toney, Z. A. Bao, *Nature* **2011**, *480*, 504.

[26] *Physics of Semiconductor Devices*, (Ed: S. M. Sze), John Wiley & Sons, New York **1981**.

[27] G. R. Hutchison, M. A. Ratner, T. J. Marks, *J. Am. Chem. Soc.* **2005**, *127*, 16866.

[28] R. P. Ortiz, J. Casado, V. Hernandez, J. T. L. Navarrete, J. A. Letizia, M. A. Ratner, A. Facchetti, T. J. Marks, *Chem.-Eur. J.* **2009**, *15*, 5023.

[29] H. Okamoto, N. Kawasaki, Y. Kaji, Y. Kubozono, A. Fujiwara, M. Yamaji, *J. Am. Chem. Soc.* **2008**, *130*, 10470.

Adv. Funct. Mater. **2013**,
DOI: 10.1002/adfm.201203439